Wave guiding in fractured layered media

S. SHAO[1]*, C. L. PETROVITCH[2] & L. J. PYRAK-NOLTE[1,3,4]

[1]*Department of Physics, Purdue University, West Lafayette, IN 47906, USA*

[2]*Applied Research Associates Inc., Raleigh, NC 27615, USA*

[3]*Department of Earth, Atmospheric and Planetary Sciences, Purdue University, West Lafayette, IN 47906, USA*

[4]*School of Civil Engineering, Purdue University, West Lafayette, IN 47906, USA*

**Corresponding author (e-mail: shao5@purdue.edu)*

Abstract: Many carbonate rocks are composed of layers and contain fracture sets that cause the hydraulic, mechanical and seismic properties to be anisotropic. Co-located fractures and layers in carbonate rock lead to competing wave-scattering mechanisms: both layers and parallel fractures generate compressional-wave (P-wave) guided modes. The guided modes generated by the fractures may obscure the presence of the layers. In this study, we examine compressional-wave guided modes for two cases: wave guiding by fractures in a layered medium with sub-wavelength layer thickness; and wave guiding in media with competing scattering mechanisms, namely layering (where the thickness is greater than a wavelength) and parallel sets of fractures. In both cases, the fracture spacing is greater than a wavelength. When the layer thickness is smaller than a wavelength, P-wave guiding is controlled by the spacing of the fractures, fracture specific stiffness, the frequency of the signal and the orientation of the layering relative to the fracture set. The orientation of the layering determines the directionally dependent P-wave velocity in the anisotropic matrix. When the layer thickness is greater than a wavelength and an explosive point source of a signal is located in the layer containing a fracture, the fracture either enhanced or suppressed compressional-mode wave guiding caused by the layering in the matrix.

Carbonate reservoirs pose a scientific and engineering challenge to geophysical prediction and monitoring of fluid flow in the subsurface. This is particularly true for carbonate rocks, many of which form in spatially and temporally variable depositional environments, and are modified further by diagenesis and deformation during the subsequent rock history. Variations in primary depositional geometries (metre to kilometre scale), as influenced by factors such as their depositional environments, sea-level fluctuations and climate, are reflected by distinct stacking patterns of rock layers or bodies, and variations in their thickness and lateral continuity. Depositional and/or construction processes influence finer-scale (micron to centimetre scale) textural variations and the formation of sedimentary structures. The resulting pore systems in the rock matrix comprise pores that vary in scale from submicron to centimetres. Fossil and primary mineral content, as well as spatial and compositional variations in cements, introduce further heterogeneities to the rock texture. Both cements and pore structure can be modified multiple times by temporal variations in the compositions, temperatures and flow rates of fluids migrating through the rocks. Carbonate rocks that have been subjected to deformation in response to burial, tectonic and induced (e.g. during hydrocarbon production) stresses commonly develop arrays of fractures as well as stylolites. While the orientations of these features vary with the burial and deformation history, fracture arrays are commonly steeply dipping, while stylolites tend to be oriented parallel to bedding.

Difficulties in interpreting subsurface data from carbonate reservoirs and aquifers are increased by the fact that their geological features span a wide spectrum of length scales and form over a wide range of timescales. The hierarchy of processes that generate the geological features in carbonate rocks (e.g. stacking patterns of strata and their continuity, diagenetic geobodies, hardgrounds, fractures, stylolites, and faults) generate features that overlap in their length scales. This geological 'blurring' makes it particularly difficult to isolate the discrete elements at a given scale that form the building blocks of features at larger scales. Thus, an accurate geophysical assessment of the flow behaviour of carbonate reservoirs requires a fundamental understanding of the interplay of the physical processes that act over multiple timescales to form multiscale rock fabrics. The geological features that contribute to these fabrics impact flow behaviours and geophysical signatures over various length scales.

From: AGAR, S. M. & GEIGER, S. (eds) 2015. *Fundamental Controls on Fluid Flow in Carbonates: Current Workflows to Emerging Technologies*. Geological Society, London, Special Publications, **406**, 375–400.
First published online June 2, 2014, http://dx.doi.org/10.1144/SP406.8

This paper focuses on just two components of carbonate rocks that affect seismic interpretation of the physical properties of carbonates, namely, the effect of layering in the rocks and a set of parallel fractures. In this study, fracture orientation is either parallel to the strike and dip of the layering (i.e. fractures are oriented parallel to the layering), or the fracture strike and dip are perpendicular to the layering (i.e. fracture sets are perpendicular to the layering). The effect of layering on seismic wave propagation depends on the thickness of the layers relative to a wavelength. Layers are assumed to represent an impedance contrast or change in mechanical properties relative to the surrounding layers. The source of the material contrast may arise from different texture porosity, mineralogy, cement or microcrack distribution or orientation (Boggs 2006). When the layer thickness in a carbonate is much smaller than a wavelength – that is, $d'/\lambda \ll 1$, where d' is the layer thickness and λ is the wavelength (Backus 1962; Sheriff & Geldart 1995) – the rock can be treated as a transversely isotropic (TI) medium. In more complex settings, the local stress distribution can result in orthorhombic behaviour, such that the velocity varies in all three directions because of layering and preferential microcrack closure or opening. When the thickness of the layers is comparable to an integer multiple of a wavelength, wave guiding can occur as a result of different acoustic impedance between layers for the P-wave (compressional) and S-wave (shear) (Li 2011). This will lead to energy confinement within layers and interference between the direct mode and modes internally reflected within layers.

The effect of thick layers (i.e. greater than a wavelength) on P-waves is shown in Figure 1. Li *et al.* (2009) performed acoustic wavefront imaging on a $100 \times 100 \times 100$ mm cubic sample of Austin Chalk to obtain a three-dimensional (3D) ($X \times Y \times t$) dataset of the compressional wavefront: the dimensions of a rectangular scanned region are X mm $\times$ Y mm, with data acquired in 1 mm increments in each direction. A total number of $X \times Y$ waveforms were collected. Each waveform contained t data points of amplitudes. Figure 1 contains 2D slices ($X \times t$) from a 3D dataset collected on Austin Chalk. One spatial dimension (slices on face E) and one temporal direction (time axis) are shown for locations $Y = 10$–58 mm. Acoustic wavefront imaging uses a spherical source (Roy & Pyrak-Nolte 1995; Wolfe 1995; Xian *et al.* 2001; Oliger *et al.* 2003). If the rock had been isotropic, the wavefront would have spread out uniformly (spherically) in space as a function of time. In Figure 1, the variation in the arrival time of the direct P-wave is observed to be non-uniform. The non-uniformity is caused by the large layers in the sample. Li *et al.* (2009) determined that the density among the layers in a companion Austin Chalk sample varied from 1700 to 2300 kg m^{-3}, while the P-wave velocity varied by 16% throughout locations in the X mm $\times$ Y mm region of the sample. The difference in velocity among the layers in their Austin Chalk sample produced signatures of wave guiding. For example, in the slice from the 30 mm location, strong wave-guiding signatures were observed at positions between 10 and 20 mm, 30 and 40 mm, and 50 and 60 mm (Fig. 1, such as strong energy confinement and multicycles of signals). Specifically, multiple oscillations are observed with the dominant energy (red in Fig. 1) arriving after the first arrival. Thus, layering in Austin Chalk is sufficient to produce guided modes on the laboratory scale. These guided modes are leaky modes because of energy loss that occurs upon reflection at the boundary between layers (Aki & Richards 2005). At field-scale frequencies, the layers in this rock would be sub-wavelength, and wave guiding would not occur. However, if fractures are present and are more widely spaced (e.g. *c.* 30–60 m fracture spacing for 100 Hz signals), guided modes could exist.

In this paper, we present a theoretical, experimental and numerical study of wave guiding in fractured layered media for two specific cases: (1) fractured media with sub-wavelength layer thickness (referred to as the sub-wavelength layers); and (2) fractured media with layer thicknesses that are comparable to a wavelength. In both cases, the fracture spacing, which is defined as the perpendicular distance between two parallel fractures, is always greater than a wavelength. In the next section (‘Fractured media with sub-wavelength layer thickness’), we present a theoretical and experimental study of wave guiding between fractures in a transversely isotropic (TI) material with sub-wavelength layer thickness. In the section on ‘Fractured media with layer thicknesses greater than a wavelength’, a numerical study is introduced to determine whether a set of parallel fractures in a medium featuring periodic isotropic layers, whose thicknesses are comparable to a wavelength, can enhance or suppress wave guiding that arises from layers.

Fractured media with sub-wavelength layer thickness

Carbonate rocks are often anisotropic because of layering and commonly contain fractures that are typically vertical or sub-vertical. Many of these fractures will interconnect causing further complexity. Horizontal fractures are less common but can form during partial uplift of buried sequences

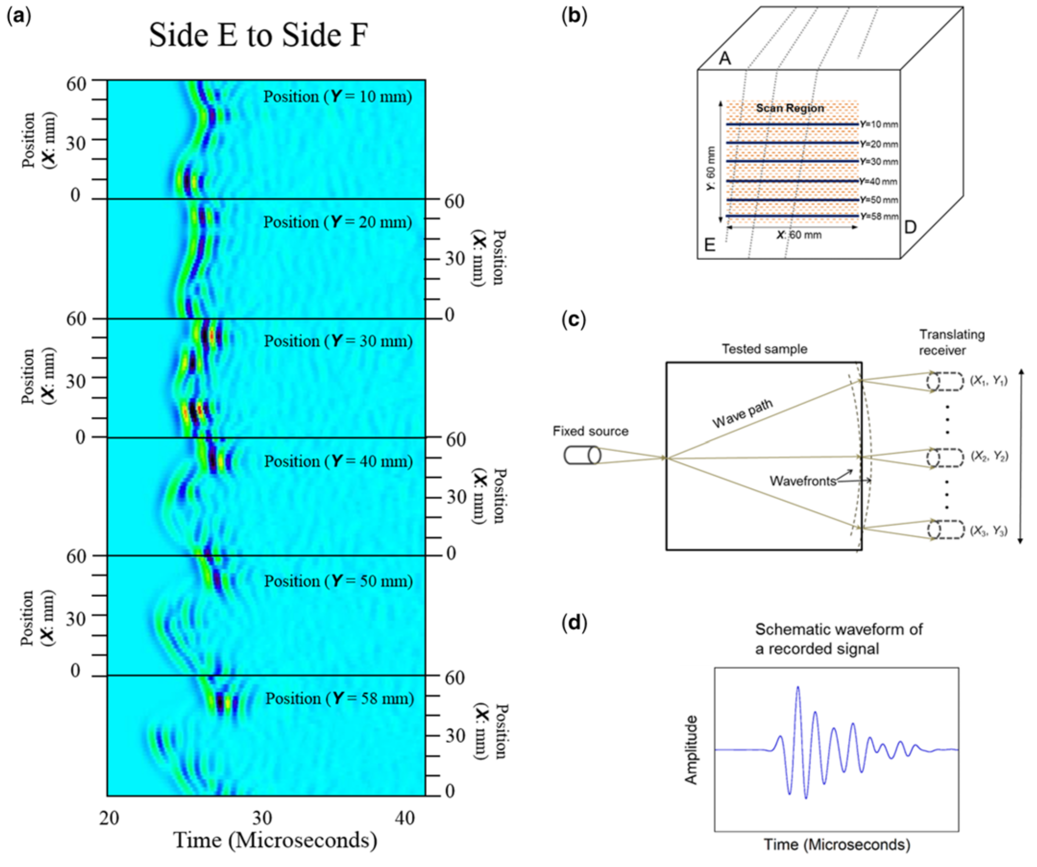

Fig. 1. (**a**) Acoustic wavefronts from a sample of Austin Chalk that were transmitted from Face E to Face F (opposite to Face E). A 20 µs window (X–t) of wavefronts recorded over a 60 mm (X) × 60 mm (Y) region is shown for slices from the 3D dataset for positions $Y = 10$, 20, 30, 40, 50 and 58 mm that are taken perpendicular to the layering on Face E. Colour represents the amplitude of the signal. A sketch of the sample with the X and Y directions are shown in (**b**). The dotted lines in (b) indicate the approximate orientation of the layers in the sample. A sketch of the measurement technique and a recorded signal are presented in (**c**) and (**d**), respectively.

owing to the removal of overburden or in compressional tectonic settings (Fatemi & Kharrat 2012). In this study, two fracture orientations with respect to the layering were selected that represent the end members of the many complex situations that may occur in carbonate rocks. These end members are (Fig. 2): (1) a medium with fractures oriented perpendicular to the layers and referred to in this paper as the FV medium (Fig. 2a); and (2) a medium with fractures oriented parallel to the layers and referred to as the FH medium (Fig. 2b). The presence of a set of parallel fractures in a transversely isotropic (TI) medium can produce P-wave (compressional wave) guided modes and energy confinement. In this section, we demonstrate that the number of modes, the time delay for different P-wave guided modes and the phase shifts depend on the orientation of the fractures relative to the matrix layering. A theoretical derivation of P-wave guided modes between fractures in a TI medium with sub-wavelength layers is presented followed by experimental observations.

Theory: wave guiding between fractures in an anisotropic medium

A monochromatic plane wave with wavelength λ and phase velocity v propagates in the x–z plane with a reflection angle of θ, with respect to the z-axis (Fig. 3). The plane wave reflects between the upper and lower fracture planes as it propagates. The wave-guiding condition (Saleh & Teich 1991) requires constructive interference after each reflection (i.e. twice reflected). This action results in two distinct plane waves: the original wave and the twice-reflected wave (Fig. 3). Waves that satisfy this

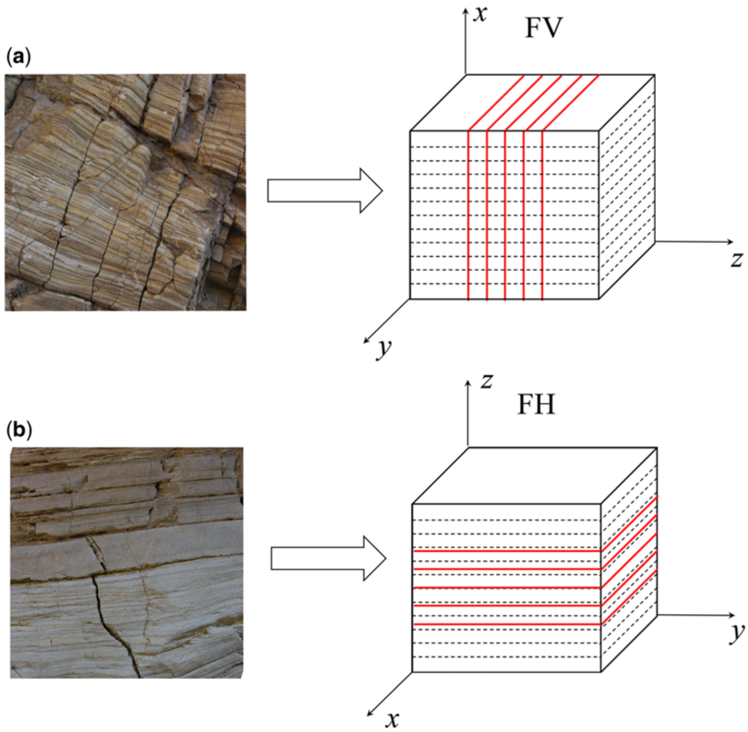

Fig. 2. (**a**) A photograph of fractures oriented perpendicular to the layering and a sketch of the FV medium representing the end members of this case in this study. (**b**) A photograph of fractures oriented parallel to the layering and a sketch of the FH medium used in this study. In the sketches of the FV and FH media, the thick solid lines represent the fractures and the thin dashed lines represent the layers. The images were taken by the author in Mosaic Canyon in Death Valley National Park, California, USA.

condition are called guided modes (or eigenmodes). This wave-guiding condition can be expressed as:

$$\frac{2\pi(\mathrm{AC}-\mathrm{AB})}{\lambda}+2\phi_{\mathrm{Rpp}}=2\pi m \qquad (1)$$

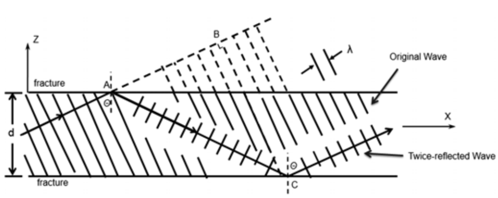

Fig. 3. Ray paths (arrows) of a wave guided between two parallel fractures for sub-wavelength layers in the x–z plane (the y-direction is into the page). The fracture planes are parallel to the x–y plane. For the fractured TI media with fine sub-wavelength layering, the layering planes either lie in the x–y plane, parallel to the fractures (the FH medium), or in the x–z plane vertical to the fracture (the FV medium). The wave front is perpendicular to the ray path. λ represents the wavelength, θ represents the reflection angle with respect to the z-axis.

where m is a non-negative integer, AC and AB are the distances from A to C and from A to B, and ϕ_{Rpp} is the phase shift calculated from the complex reflection coefficient for the P-wave. Equation (1) is the condition for perfect constructive interference. Geometrically, AC and AB are related through:

$$\mathrm{AC}-\mathrm{AB}=2\,d\cos\theta \qquad (2)$$

where d is the spacing between two fractures (Fig. 3). Once the P-wave reflection coefficient for a fractured TI medium is obtained, the mode number, m, can be calculated numerically for the reflection angle, θ, from 0° to 90° (Xian *et al.* 2001).

The reflection coefficient is derived for a P-wave incident upon a fracture in a TI medium based on the work of Carcione & Picotti (2012). A fracture is represented by a set of boundary conditions that is often referred to as the displacement discontinuity theory or the linear-slip theory (Murty 1975; Schoenberg 1980; Kitsunezaki 1983; Pyrak-Nolte *et al.* 1990*a*, *b*). These boundary conditions are: (1) the stress is continuous across a fracture; and (2) the discontinuity in displacement across the fracture is inversely proportional to the specific stiffness of the fracture. Fracture specific stiffness depends on the size and spatial distribution of the aperture and contact area within a fracture (Barton *et al.* 1985; Brown & Scholz 1985; Brown *et al.* 1986; Hopkins *et al.* 1987; Hopkins 1990; Hopkins *et al.* 1990; Pyrak-Nolte & Morris 2000; Lubbe *et al.* 2008; Petrovitch *et al.* 2013). As a fracture opens or closes in response to changes in stress, the fracture specific stiffness changes because the contact area and aperture distribution are altered. Thus, seismic wave transmission and reflection, as well as group time delays, are affected by changes in fracture specific stiffness. In most conditions, wave guides formed by parallel fractures are leaky (Nihei *et al.* 1999) because energy is lost every time a wave reflects off a fracture. The amount of energy loss depends on the frequency of the signal and the fracture specific stiffness (Xian *et al.* 2001).

The following derivation is for P-wave guided modes in the FH medium, which has a vertical symmetry axis perpendicular to the horizontal layers (the z-direction in Fig. 2). P-wave propagation is taken to be in the x–z plane (Fig. 2). For an FH medium, the elastic stiffness tensor C for a TI background is expressed as:

$$C=\begin{pmatrix} C_{11} & C_{11}-2C_{66} & C_{13} & 0 & 0 & 0 \\ C_{11}-2C_{66} & C_{11} & C_{13} & 0 & 0 & 0 \\ C_{13} & C_{13} & C_{33} & 0 & 0 & 0 \\ 0 & 0 & 0 & C_{44} & 0 & 0 \\ 0 & 0 & 0 & 0 & C_{44} & 0 \\ 0 & 0 & 0 & 0 & 0 & C_{66} \end{pmatrix}. \tag{3}$$

For convenience, Voigt's notation has been applied to convert the tensor into a second rank matrix (e.g. $1123 \longrightarrow 14$, see Thomsen 1986).

When only the in-plane P-SV wave propagation is considered (no SH-wave, and no y-component of displacement), the displacements on the upper and lower surfaces of a fracture are written as:

$$\begin{aligned} u^{(1)} &= u_{\mathrm{PI}} + u_{\mathrm{PR}} + u_{\mathrm{SR}} \\ u^{(2)} &= u_{\mathrm{PT}} + u_{\mathrm{ST}} \end{aligned} \tag{4}$$

where superscripts (1) and (2) indicate displacements in the upper and lower media of the fracture, subscripts (I, R, T) represent the incident, reflected and transmitted waves, and subscripts (P, S) represent the P-wave and SV-wave.

Carcione & Picotti (2012) derived the matrix equation for the reflection and transmission coefficients for a fracture in a TI medium:

$$\begin{pmatrix} \beta_{\mathrm{P1}} - c_x W_{\mathrm{P1}} & \beta_{\mathrm{S1}} - c_x W_{\mathrm{S1}} & -\beta_{\mathrm{P2}} & -\beta_{\mathrm{S2}} \\ \xi_{\mathrm{P1}} - c_z Z_{\mathrm{P1}} & \xi_{\mathrm{S1}} - c_z Z_{\mathrm{S1}} & \xi_{\mathrm{P2}} & \xi_{\mathrm{S2}} \\ Z_{\mathrm{P1}} & Z_{\mathrm{S1}} & -Z_{\mathrm{P2}} & -Z_{\mathrm{S2}} \\ W_{\mathrm{P1}} & W_{\mathrm{S1}} & W_{\mathrm{P2}} & W_{\mathrm{S2}} \end{pmatrix} \times \begin{pmatrix} R_{\mathrm{PP}} \\ R_{\mathrm{PS}} \\ T_{\mathrm{PP}} \\ T_{\mathrm{PS}} \end{pmatrix} = \begin{pmatrix} -\beta_{\mathrm{P1}} - c_x W_{\mathrm{P1}} \\ \xi_{\mathrm{P1}} - c_z Z_{\mathrm{P1}} \\ Z_{\mathrm{P1}} \\ W_{\mathrm{P1}} \end{pmatrix} \tag{5}$$

where normal stress $\sigma_{zz} = Z$, tangential stress $\sigma_{zx} = W$, β and ξ are vertical and horizontal plane wave polarization components that relate to the directionally dependent S- and P-wave velocities, and $c_a (a = x, z)$ is the inverse of the normal or tangential fracture stiffness (i.e. compliance). The reflection coefficient R_{PP} is obtained numerically by solving equation (5).

In an FV medium, the fractures lie in the x–y plane, while the normal to the layers is in the x-direction (Fig. 2). The stiffness tensor for an FV medium is:

$$C=\begin{pmatrix} C_{11} & C_{12} & C_{11}-2C_{55} & 0 & 0 & 0 \\ C_{12} & C_{22} & C_{12} & 0 & 0 & 0 \\ C_{11}-2C_{55} & C_{12} & C_{11} & 0 & 0 & 0 \\ 0 & 0 & 0 & C_{44} & 0 & 0 \\ 0 & 0 & 0 & 0 & C_{55} & 0 \\ 0 & 0 & 0 & 0 & 0 & C_{44} \end{pmatrix}. \tag{6}$$

The P-wave reflection coefficient, R_{PP}, for the FV medium is calculated by using equation (5).

Xian *et al.* (2001) derived the solution for compressional-mode wave guiding between fractures in an isotropic medium, and found that the number of modes generated depends on the frequency of the signal and the fracture specific stiffness. From our derivation for wave guiding between parallel fractures in a TI medium, the number of modes is shown to also depend on the frequency and fracture specific stiffness. Moreover, the number of modes is also affected by the orientation of the layers relative to the fractures because of the difference in the values of the elastic constants of the matrix (Fig. 4). Figures 4–9 are theoretical results based on the material properties of the FH and FV garolite samples, which are epoxy-cloth laminates with fine sub-wavelength layering used in the experiments. The material properties are given

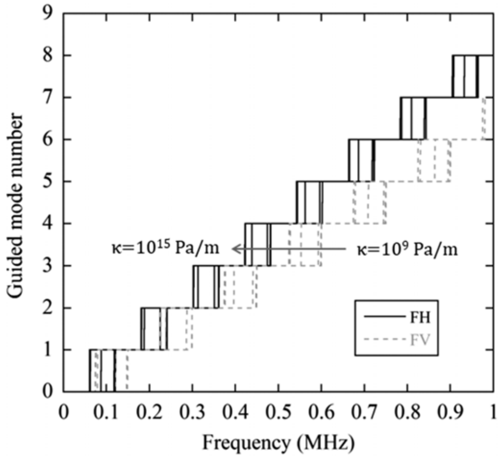

Fig. 4. Number of guided modes (m) for media FH and FV as a function of frequency and for a range of fracture specific stiffness ($\kappa = 10^9$–10^{15} Pa m^{-1}).

in Table 1 for the experimental frequency range. Figure 4 shows the number of guided modes for the FH and FV media that satisfy equation (1) as a function of frequency for selected stiffnesses (shear stiffness and normal stiffness are assumed to be equal) from 10^9 to 10^{15} Pa m^{-1}.

As shown in Figure 4, for the same frequency and fracture specific stiffness range, fewer modes are generated for FV than for FH. For the FH medium, no guided mode exists when the frequency is lower than 0.05 MHz. However, guided modes exist for frequencies higher than 0.07 MHz for the FV medium. More modes are observed for lower fracture specific stiffness and higher frequencies because less energy is lost to transmission across the fracture upon reflection.

The group delay for guided waves arises from two aspects: geometric (when the guided wave travels a longer distance than the direct wave) and dynamic (group delay that occurs because of the phase shift upon reflection from fracture). The geometrical, t_{geo}, dynamic, t_{dyn}, and total delay, T_{total}, are expressed as:

$$
\begin{aligned}
t_{\text{geo}} &= \frac{L}{V_{\text{P}}(\theta)\sin\theta} - \frac{L}{V_{\text{P}}(\theta)} \\
t_{\text{dyn}} &= N\frac{\mathrm{d}\phi_{R\text{pp}}}{\mathrm{d}\omega} \\
T_{\text{total}} &= t_{\text{geo}} + t_{\text{dyn}}
\end{aligned}
\qquad (7)
$$

where $V_{\text{P}}(\theta)$ is the P-wave velocity as a function of reflection angle θ, $\phi_{R\text{pp}}$ is the phase shift experienced upon reflection from the fracture and N is the number of reflections within a sample of length L (with the source assumed to be at the centre of the waveguide). The dynamic time delay, t_{dyn}, depends on the phase shift upon the reflection from the fracture (equation 7). From the displacement discontinuity theory, the phase shift depends on frequency, fracture specific stiffness and the material properties of the matrix (equation 7). The geometric time delay, t_{geo}, is also affected by these same parameters through the wave-guiding requirement (equation 1).

Figure 5 shows the contributions to the total time delay (Fig. 6) from the dynamic and geometric group time delays as a function of frequency for a fracture specific stiffness of $\kappa = 10^{11}$ Pa m^{-1}. First, the orientation of the fractures relative to the layering affects the time delays because the layering produces anisotropy that affects $V_{\text{P}}(\theta)$ in equation (7) and the phase shift upon reflection. Velocities and energy partitioning of P- and S-waves are directionally dependent on the material properties in anisotropic media. The reflection angle, θ, as a function of frequency is shown in Figure 7 for a range of fracture specific stiffness for FH and FV. The number of reflections for a given sample length determines the magnitude of t_{dyn}.

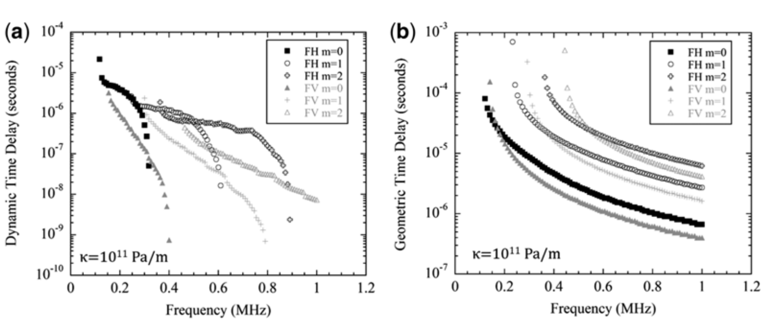

Fig. 5. (**a**) The dynamic group time delay and (**b**) the geometric group time delay as a function of frequency for modes $m = 0$, 1 and 2 for fractures parallel to the layering, FH, and for fractures perpendicular to the layering, FV, for fractures with a specific stiffness of 10^{11} Pa m^{-1}.

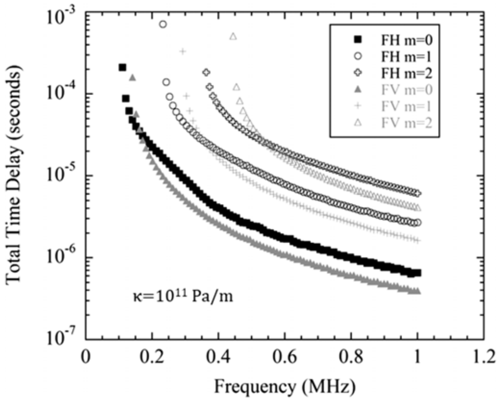

Fig. 6. Total group time delay for as a function of frequency for modes $m = 0$, 1 and 2 for fractures parallel to the layering (FH) and for fractures perpendicular to the layering (FV) for fractures with a fracture specific stiffness (κ) of 1×10^{11} Pa m^{-1}.

Secondly, both geometric and dynamic time delay components (Fig. 5), as well as the total time delay (Fig. 6), are a function of frequency because the existence of fracture guided modes (equation 1) depends on the wavelength of the signal and the fracture spacing. However, an additional frequency dependence arises from the fracture that does not occur for waves guided only by layering. A fracture that is represented as a non-welded contact produces a group time delay for both transmitted and

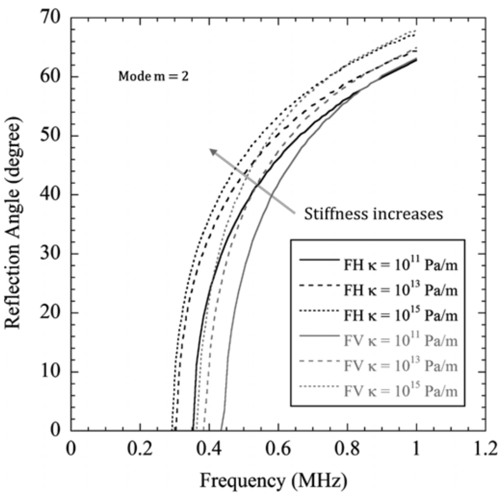

Fig. 7. Reflection angle (guided mode $m = 2$) from a fracture as a function of frequency for fractures parallel to the layering (FH) and for fractures perpendicular to the layering (FV) for a fracture specific stiffness (κ) of 10^{11}, 10^{13} and 10^{15} Pa m^{-1}.

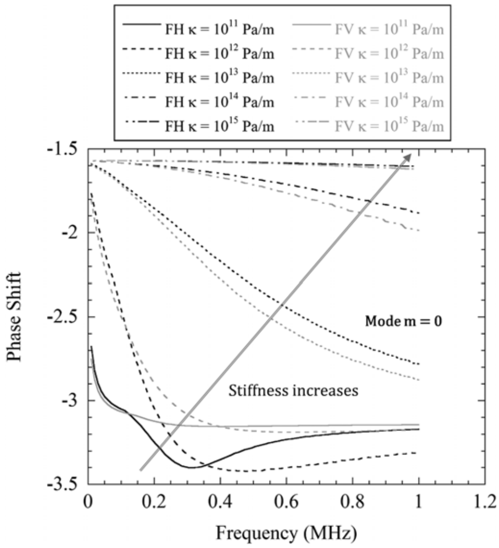

Fig. 8. Phase shift (guided mode $m = 0$) upon reflection from a fracture as a function of frequency for a range of fracture specific stiffness for fractures parallel to the layering (FH) and for fractures perpendicular to the layering (FV) for a fracture specific stiffness (κ) of 10^{11}, 10^{12}, 10^{13}, 10^{14} and 10^{15} Pa m^{-1}.

reflected waves. The dynamic time delay, t_{dyn}, is found by taking the change in phase as a function of frequency. The presence of a fracture results in a P-wave reflection phase shift (ϕ_{Rpp}) that is a function of frequency and fracture specific stiffness. Figure 8 illustrates the dependence of the phase shift upon reflection on signal frequency and on

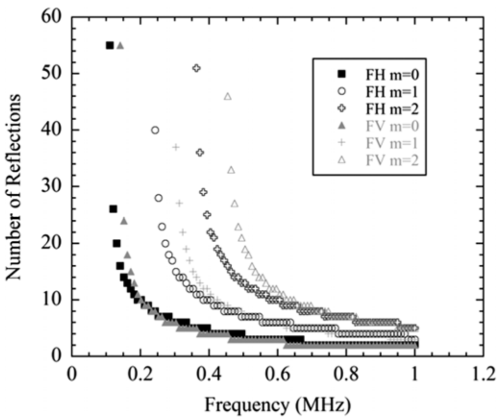

Fig. 9. Number of reflections (bounces) as a function of frequency for modes $m = 0$, 1 and 2 for fractures parallel to the layering (FH) and for fractures perpendicular to the layering (FV) for fractures with a fracture specific stiffness (κ) of 10^{11} Pa m^{-1}.

Table 1. *Material properties*

Properties	FH	FV
C_{11} (GPa)	13.76	11.71
C_{13} (GPa)	3.92	6.43
C_{33} (GPa)	7.71	11.71
C_{44} (GPa)	2.44	2.34
C_{55} (GPa)	2.44	2.64
C_{66} (GPa)	3.11	2.34
ρ (kg m^{-3})	1327	1301

Elastic stiffness components, C, and density of the matrix, ρ, for FH (fractures and layers are parallel) and FV (fractures are perpendicular to the layering) media.

fracture specific stiffness, as well as on the fracture orientation relative to layering. A fracture represented as a displacement discontinuity boundary acts as a low-pass filter. As the stiffness of the fracture increases, more high-frequency components of the signal are transmitted across the fracture, and less of the reflected energy is trapped within the wave guide formed by the parallel fractures. It is noted that lower fracture stiffness results in a rapid change in the phase shift as a function of the signal frequency, which increases the magnitude of dynamic delay of a single reflection (Fig. 8).

Finally, like the isotropic case of wave guiding between parallel fractures, high mode numbers experience greater time delays (Figs 4 & 5) than lower mode numbers because the number of reflections from the fractures increases as m increases (Fig. 9). The number of reflections increases because the reflection angle approaches normal incidents ($\theta \longrightarrow 0°$) as the frequency decreases.

The theoretical analysis presented here demonstrates that a TI matrix with sub-wavelength layers affects the time delay of waves guided between parallel fractures because of the directionally dependent P-wave and S-wave velocities. In the next subsection, we describe the experimental approach used to measure and observe wave guiding between fractures in an anisotropic medium.

Experimental set-up

Wavefront imaging experiments were performed to capture the spatial distribution of energy with time in garolite samples that simulated fractured rock with sub-wavelength layers. Garolite is an epoxy-cloth laminate that can be considered transversely isotropic and has layers approximately 0.5 mm thick. Three cubic samples were studied. Samples FV (Fig. 2a) and FH (Fig. 2b) each contained five parallel fractures with a fracture spacing of 10 mm (approximately 3λ–3.3λ, where λ is the wavelength of the P-wave, around 3 mm at 1 MHz). An intact sample containing no fractures was used as a control. Synthetic fractures were created by cutting the samples with a band saw and then belt-sanding the surfaces. In the FH sample, the fracture set was oriented parallel to the layering, while, for the FV, the fractures were oriented perpendicular to the layering, as described in the previous subsection. Both fractured samples were sealed by placing crystal-clear tape on all surfaces of a sample. The sample dimensions were approximately 102 × 102 × 102 mm.

A wavefront imaging system (Fig. 10) was used to characterize the samples and to capture P-wave guided modes. The system includes: (1) ultrasonic transducers to send and receive signals; (2) a pulse generator; (3) motion controllers for 1D–3D data acquisition; (4) an oscilloscope; (5) a digitizer; and (6) a computer. Two water-coupled spherically focused piezoelectric transducers (Panametrics V303S-SU) were used in this experiment with a central frequency of 1 MHz and a nominal element size of 13 mm. Water-coupling ensured

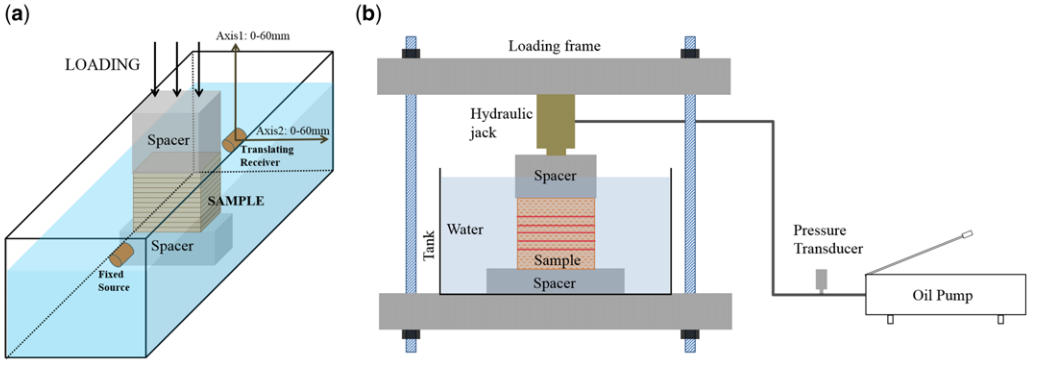

Fig. 10. (**a**) Schematic of wavefront imaging system showing the location of transducers, translation directions and sample in the water tank. (**b**) Schematic of the loading system used during wavefront imaging.

the same coupling between the transducer and sample at all locations. After sealing a sample with tape, the sample was placed between platens in a tank of water (Fig. 10). Up to 45 kN of normal load was applied to a sample with a manual hydraulic pump (ENERPAC P80V). A pressure transducer (Transmetric P115CG) was used to monitor the pressure during the experiment.

To record a wavefront imaging dataset in the same manner as that from the experiment in Li *et al.* (2009) (see the introduction of this paper), the source transducer was maintained at a fixed location, while the receiver was used to record data over a 2D region to obtain the spatial distribution of energy with time. Each sample was scanned over a 60 × 60 mm region in 1 mm increments to map out the arriving wavefront (i.e. 3600 transmitted waveforms were recorded). This procedure resulted in a 3D dataset: two spatial dimensions and one temporal dimension. Both the source and receiver transducers were focused on the surface of the sample, with an approximate focal distance of approximately 18.2 mm (from the centre of the transducer to the edge of the sample). The beam diameter for this distance was about 2.1 mm. The beam diameter is defined as the transverse distance between two points where the signal amplitude is 50% (−6 dB) of the peak in signal amplitude.

A pulse generator (Panametrics model 5077PR) was used to input a negative (100 V) electrical square pulse into the source transducer. The pulse width was 0.3 μs, with a repetition rate of 100 Hz. Two computer-controlled linear actuators (Newport model 850B) were used to translate the receiver both horizontally and vertically. Waveforms were collected from the receiver transducer by a digital oscilloscope (LeCroy 9314L) and were stored on a computer for analysis. For each transducer combination, a 100 μs window of the waveform, with a time delay of 43 μs, was recorded with a resolution of 0.01 μs per point (10 000 points per signal).

A set of calibration experiments were performed to assess the ability of using wavefront imaging to extract quantitative information on the velocity anisotropy of a sample. Figure 11 shows snapshots (2D: 60 × 60 mm) of wavefronts recorded for a transparent acrylic sample (Fig. 11a) and a phenolic G10 sample (Fig. 11b) that is a fibreglass laminate. The acrylic sample was isotropic, and the wavefront in Figure 11 is circular because the P-wave propagates with the same speed in all directions. The phenolic G10 sample is a tight fibre-glass laminate with a unique vertical direction, which is expected to behave as an example of VTI media. The wavefronts in the G10 sample are elliptical because the P-wave propagates faster parallel to the layers (horizontal axis in Fig. 11b) than perpendicular to the layers. The P-wave velocity ratio ($V_{P\parallel}/V_{P\perp}$) for the acrylic and G10 samples were 1.04 and 1.24, respectively, and match the ratios determined from traditional contact transducer measurements made for three orthogonal directions.

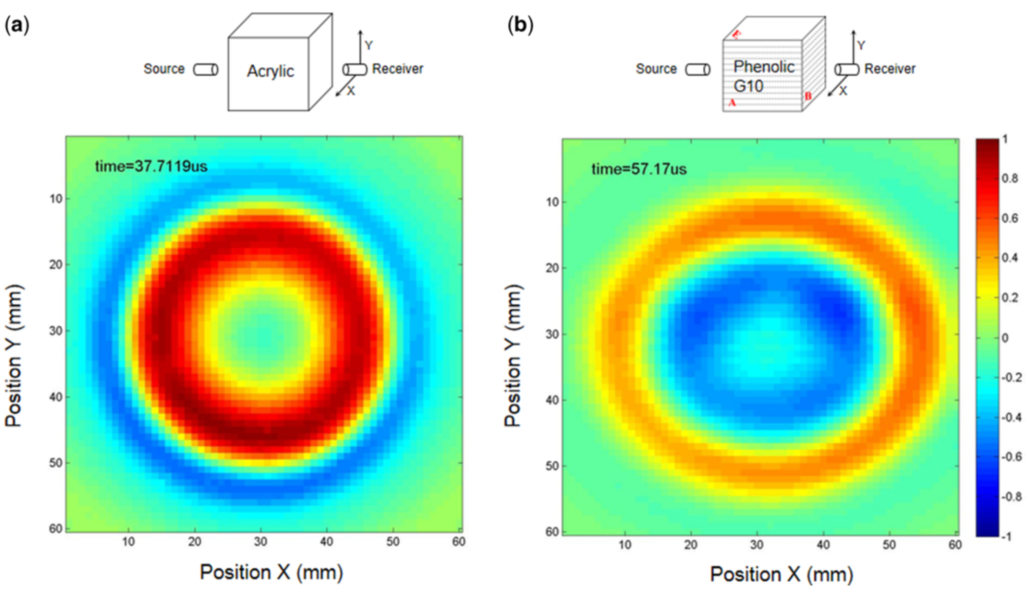

Fig. 11. 2D snapshots of wavefronts from (**a**) an isotropic acrylic sample and (**b**) a VTI phenolic G10 sample. The colours in the snapshots represent the amplitudes of the received signals at a certain time.

Experimental results

Wavefront imaging results. Wavefront imaging enables characterization of the samples and imaging of guided modes. The anisotropy of the Intact sample was observed in the wavefront shown in Figure 12b (top). The black dots on the signals shown in Figure 13 indicate the time of the wavefronts shown in Figure 12. The wavefronts in Figure 12b represent a 60 × 60 mm region of the sample and the colours represent the amplitude of the signal (see Fig. 13 for amplitude scale). The wavefront in the Intact sample spreads out faster in the direction parallel to the layers than perpendicular to the layers, as expected for a TI sample with no fractures. Data points from the contours of

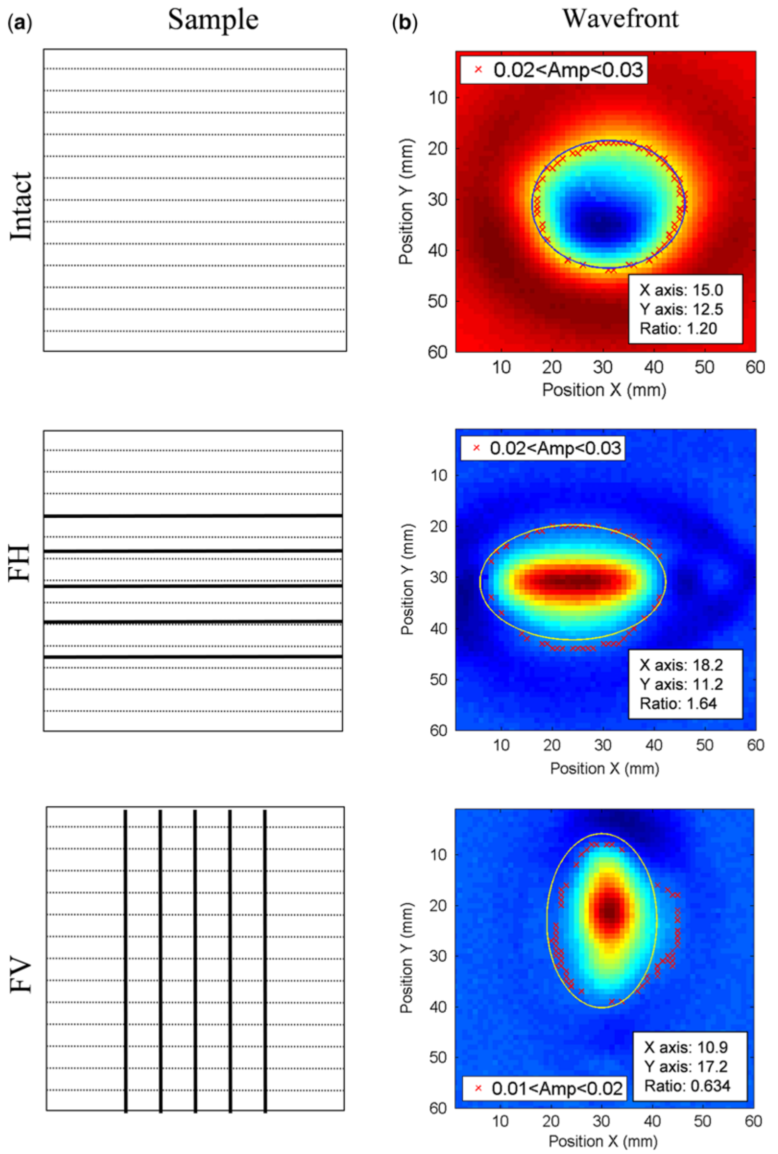

Fig. 12. (**a**) Sketch of the samples showing the orientation of the fractures (thick black lines) relative to the layering (dashed grey lines). (**b**) Contour map of signal amplitude of measured wavefronts. Samples FH and FV were subjected to a load of 45 kN applied normal to the fractures. The red crosses indicate the positions where the signal amplitudes are in desired ranges to plot the contours.

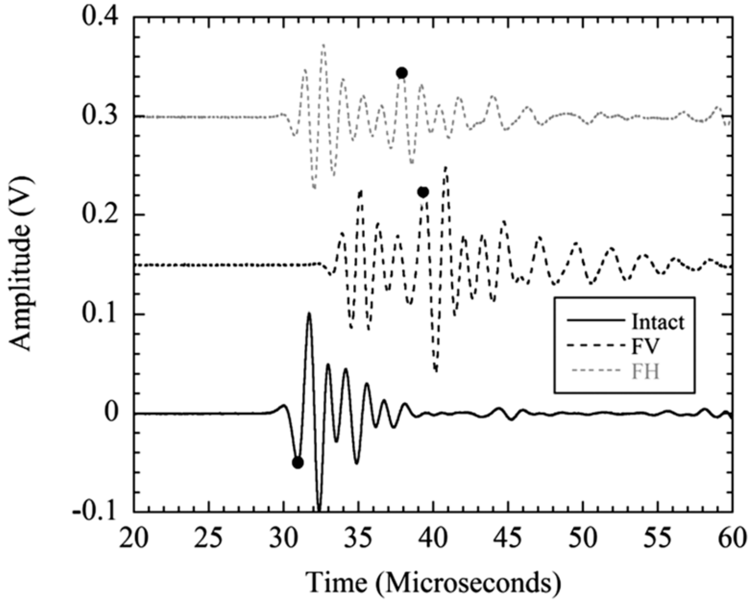

Fig. 13. Signals from the Intact sample and samples FH and FV from the centre of the wavefront imaging datasets. The black dot indicates the times of the wavefront snapshots shown in Figure 12b.

the wavefront were fitted with an ellipse to determine the anisotropy of the samples and are shown in Figure 12b. The P-wave velocity ratio ($V_{P\|}/V_{P\perp}$) in the Intact sample (velocity propagated parallel to the layering divided by velocity propagated perpendicular to the layering) is approximately 1.20 and has an eccentricity of 0.55. In this paper, the eccentricity is defined by $\sqrt{1-b^2/a^2}$, where a and b represent the major and minor axes of an ellipse, respectively. The effect of the fractures on the wavefront is clearly observed for samples FH and FV (Fig. 12b). For FH and FV samples, *apparent* P-wave velocity ratios ($V_{P\|}/V_{P\perp}$) are around 1.64 and 0.634, respectively. Apparent wave velocity ratios are used for the fractured sample because the wave velocities are affected by the number of fractures across which a wave has propagated and by the delays associated with wave guiding (see the earlier subsection on 'Theory: wave guiding between fractures in an anisotropic medium' for a discussion). However, while the eccentricities of the wavefront contours in FH and FV are essentially the same (0.793 and 0.773, respectively), the major axes differ in orientation by 90° because of the orientation of the fractures relative to the layering. For the fractured samples at low stresses, the observed apparent anisotropy is controlled by the fractures that mask the matrix anisotropy observed in the Intact sample.

Energy confinement between the central parallel fractures is observed in the wavefronts shown in Figure 14. In Figure 14, the acoustic wavefronts are shown for the two fractured samples, FH and FV, subjected to 45 kN and the Intact sample. For the fractured samples, the position axis (vertical axis) corresponds to the direction that is perpendicular to the fracture planes. For the Intact sample, the position axis is perpendicular to the layers. The colour represents the amplitude of the signal (see Fig. 13 for amplitudes). The signals shown in Figure 13 were taken from the centre of the wavefronts; that is, signals with the earliest arrivals were from the location where the receiver and source were aligned.

The strong energy confinement between fractures occurs because the fracture specific stiffness is low, resulting in low transmission across the fractures. The fracture stiffness is low because the fracture surfaces are not in sufficient contact with each other, under a no-load condition (Hopkins, 1990). For the FV sample, the dominant energy arrives (red colour in Fig. 14c) significantly later than the first arrival for the Intact or the early mode in FH. In the next subsection, we will use the theory to identify the guided modes observed in the data.

Comparison of theory and experimental results. The effect of fracture specific stiffness and the orientation of the layers relative to the fracture set on wave guiding in an anisotropic medium with subwavelength layering is examined using the signals

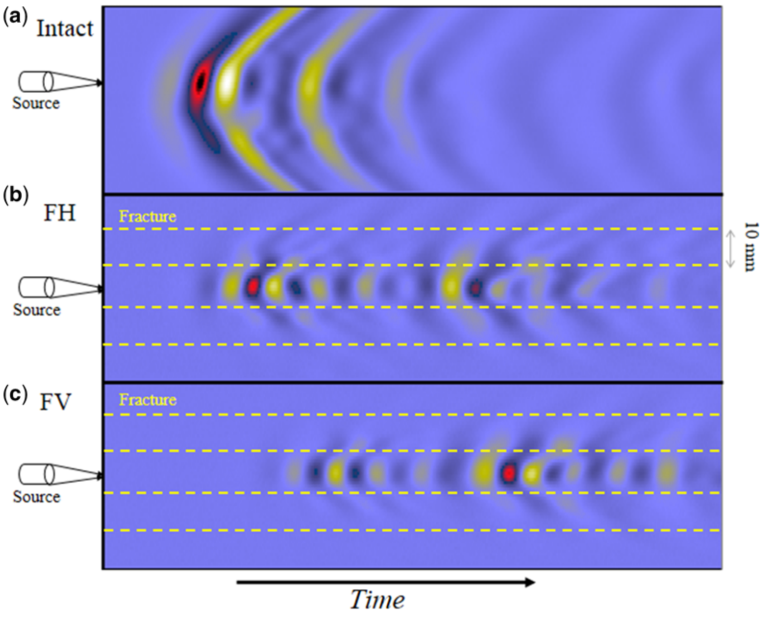

Fig. 14. Acoustic wavefronts as a function of time and position from (**a**) the Intact sample, (**b**) FH and (**c**) FV. The wavefronts for FH and FV were taken perpendicular to the fractures.

from the centre of the wavefront; that is, from between the two-parallel fractures that contained the source. Figures 15 and 16 show the received waveforms from the FH and FV samples, respectively, subjected to 0 and 4 MPa stress applied normal to the fractures. The first arrival (the direct

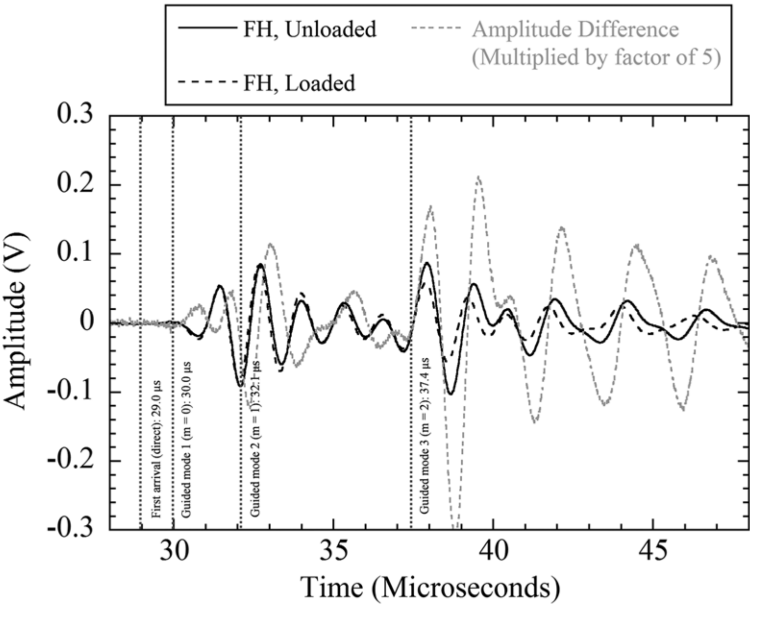

Fig. 15. Comparison of the signals from the FH sample in the unloaded and loaded (4 MPa) condition. The difference between the two signals is also shown (multiplied by a factor of 5). The arrival times of guided modes are indicated by the dotted vertical lines.

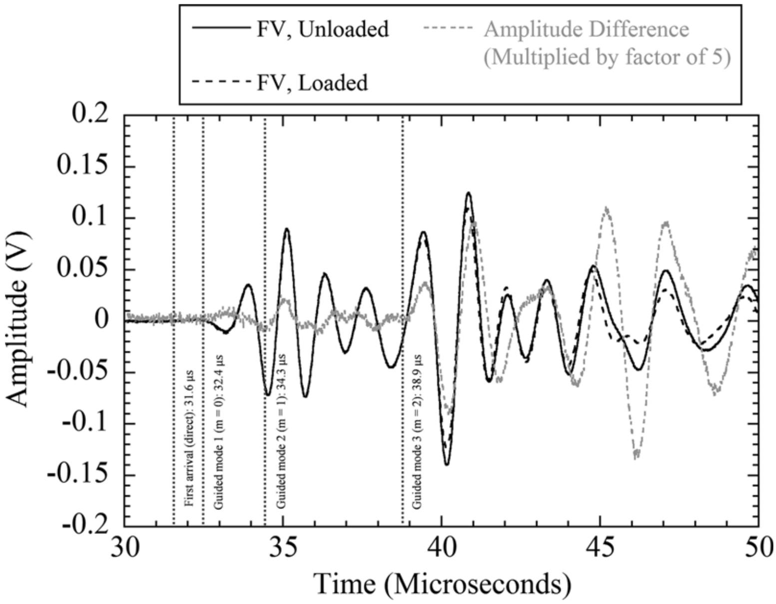

Fig. 16. Comparison of the signals from the FV sample in the unloaded and loaded (4 MPa) condition. The difference between the two signals is also shown (multiplied by a factor of 5). The arrival times of guided modes are indicated by the dotted vertical lines.

wave, identified as the onset time of the signal) is unaffected by the application of stress because at this measurement location the direct wave does not cross a fracture nor has it been reflected from a fracture. The predicted arrival times from the theory for the FH sample are listed in Table 2 for modes $m = 0$, 1 and 2. Only modes 1 and 2 are significantly affected by fracture specific stiffness for this type of frequency and material properties, because modes 1 and 2 reflect between 4 and 6 times from the fracture plane as the waves are guided, while $m = 0$ mode is only reflected twice. Thus, the additional delay produced by the fracture increases with increasing mode number (Fig. 6). If the samples were longer, the number of reflections per mode would increase and the time delay would increase. However, as mentioned earlier, a wave guide formed by parallel fractures is leaky because some loss of energy occurs each time the wave bounces off (or reflected from) a fracture. The amount of energy loss depends on the frequency of the signal and the fracture specific stiffness. Xian (2001) showed that compressional-mode guided waves were measureable for up to 15 wavelengths while preserving a significant amount of detectable energy. To help identify the guided modes, the difference between the signals from the FH sample with and without load was taken, and is shown in grey in Figure 15. As predicted by the theory, mode $m = 0$ arrives very close to the direct wave, followed by mode $m = 1$ at 32.1 μs and a clear break is identified for mode 2 at 37.4 μs. The guided modes for the FV sample did not change significantly with stress (Fig. 16) as predicted by the

Table 2. *Arrival times for Sample FH*

	Experimental	Theoretical		
Stiffness (Pa m^{-1})		10^{10}	10^{11}	10^{12}
Directional mode arrival (μs)	29.0	29.0	29.0	29.0
First guided mode $m = 0$ (μs)	30.0	30.0	30.0	30.0
Second guided mode $m = 1$ (μs)	32.1	32.9	32.9	33.3
Third guided mode $m = 2$ (μs)	37.4	38.5	38.6	40.2

Experimental arrival times of the direct and first three guided modes and their theoretical prediction as a function of fracture stiffness of the FH sample.

Table 3. *Arrival times for Sample FV*

	Experimental	Theoretical		
Stiffness (Pa m^{-1})		10^{10}	10^{11}	10^{12}
Directional mode arrival (μs)	31.6	31.6	31.6	31.6
First guided mode $m = 0$ (μs)	32.4	32.2	32.2	32.2
Second guided mode $m = 1$ (μs)	34.3	34.2	34.2	34.2
Third guided mode $m = 2$ (μs)	38.9	38.5	38.5	38.7

Experimental arrival times of the direct and first three guided modes, and their theoretical prediction as a function of fracture stiffness in the FV sample.

theory (Table 3). The theory is also used to identify the arrival of the different modes from the difference of the signals from loaded and unloaded FV sample. In Figure 16, the difference amplitude has been multiplied by a factor of 5 to clearly show the modes. Modes $m = 0$, 1 and 2 arrive near that predicted by the theory (Table 3).

A decrease in amplitude of the guided modes with stress occurred for both the FH and FV samples (Figs 15 & 16) when the samples were loaded because, as the stiffness of a fracture increases, more energy is transmitted across the fracture and less energy is confined between the fractures. Also noted is the difference in amplitude between the direct waves and guided waves ($m = 2$) for FH and FV. For the FH sample, the amplitude of the first arrival and the $m = 2$ wave are similar in magnitude. However, for the FV sample, the amplitude is greater for the guided mode $m = 2$ than the first arrival. This occurs because the total time delay for the modes $m = 0$ and $m = 2$ differs for the FH and FV media, as shown in Figure 6. The waves are phase shifted by different amounts because of the orientation of

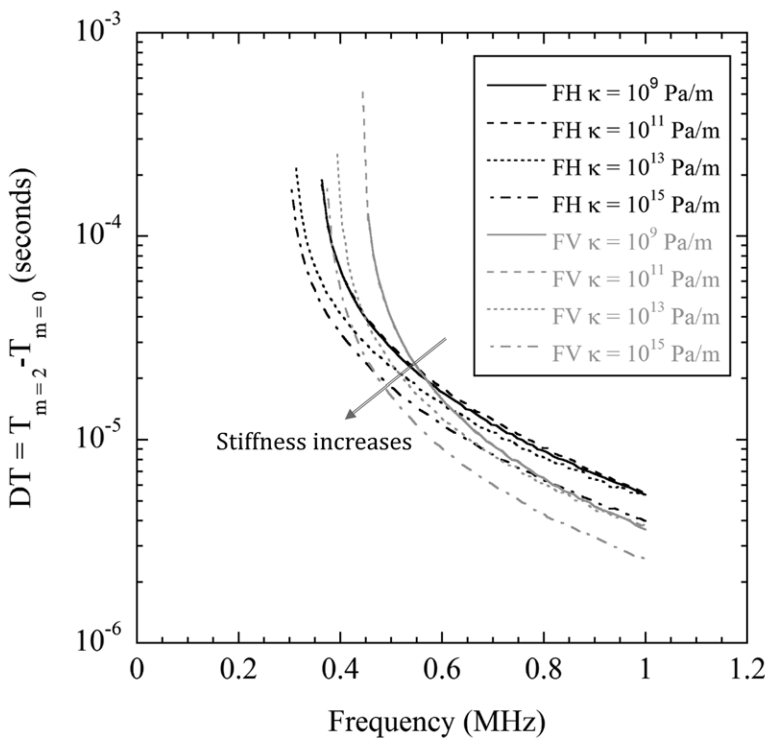

Fig. 17. The difference in total delay between mode $m = 0$ and mode $m = 2$ as a function of frequency for fractures parallel to the layering (FH) and for fractures perpendicular to the layering (FV) for a fracture specific stiffness (κ) of 10^9, 10^{11}, 10^{13} and 10^{15} Pa m^{-1}.

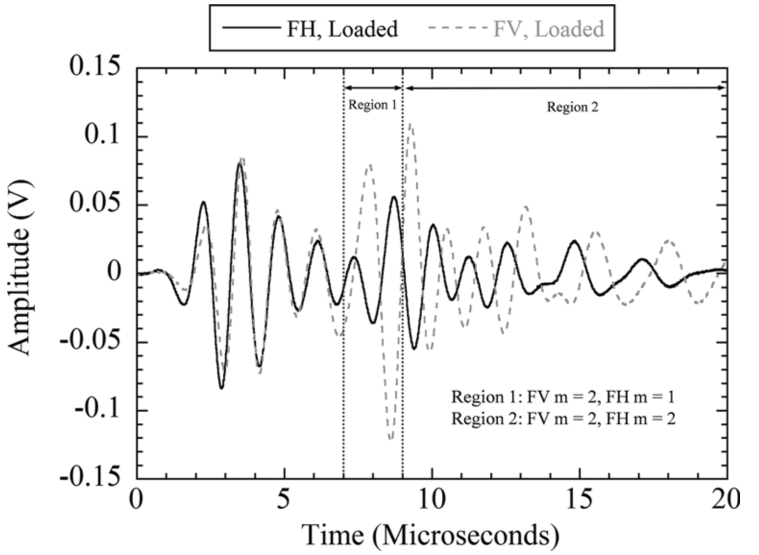

Fig. 18. Comparison of the signals from FH and FV samples when a load is applied normal to the fractures. The signals have been aligned at the first arrivals. Second guided mode in FH ($m = 1$) and third guided mode in FV ($m = 2$) occur in Region 1 (*c.* 7.0–9.0 μs later than the first arrivals), while both third guided modes ($m = 2$) occur in FH and FV in Region 2 (more than 9.0 μs later than the first arrivals).

the layers relative to the layering that results from the directional dependence of the wave velocities.

The difference in time delay between the direct wave and modes $m = 0$, 1 and 2 differs theoretically for the FH and FV samples (e.g. Fig. 17 illustrates the arrival time difference between the guided modes $m = 0$ and $m = 2$ for FH and FV, respectively). This difference is observed in the experimental data by aligning the first arrivals of signals from samples FH and FV under load (Fig. 18). The difference in time delay caused by the orientation of the layers relative to the fractures results in a phase shift between the later arriving modes of the order of 0.8π. For example, the significant shift in phase between the guided modes observed in samples FV and FH occurs because the modes arrive at different times relative to the direct wave for the samples as a result of the orientation of the layers relative to the fractures. In the signals, a significant phase shift was found around 7.0 μs later than the first arrival (Fig. 18). In the region of 7.0–9.0 μs (relative to the first arrivals), guided mode $m = 2$ arrives in the FV sample, while guided mode $m = 1$ arrives in FH. In the region from 7.0 to 9.0 μs, the total phase shift difference for these two samples is around 0.8π. In the region beyond 9.0 μs, guided mode $m = 2$ exists in both samples, and the total phase shift difference is also around 0.8π. Table 4 includes the theoretical prediction of relative phase shift between FH and FV samples. From the theory, the stiffness of the fracture is estimated to be between 1.5×10^{11} and 5.5×10^{11} Pa m^{-1}. Figure 18 also illustrates the difference in energy partitioning for

Table 4. *Phase shift between signals from FH and FV*

Fracture stiffness ($\times 10^{11}$ Pa m^{-1})	Relative phase shift in Region 1 (π)	Relative phase shift in Region 2 (π)
1.0	0.86	0.21
1.5	0.79	0.30
2.0	0.73	0.39
2.5	0.68	0.47
3.0	0.62	0.56
3.5	0.57	0.62
4.0	0.54	0.68
4.5	0.51	0.72
5.0	0.48	0.77
5.5	0.46	0.82
6.0	0.44	0.85
6.5	0.42	0.87
7.0	0.42	0.89
7.5	0.41	0.92
8.0	0.41	0.93
8.5	0.41	0.94
9.0	0.41	0.95
9.5	0.41	0.96
10.0	0.42	0.96

Relative phase shift (theory) between guided FV and FH samples in Region 1 (7–9 μs later than the first arrivals), and Region 2 (more than 9 μs later than the first arrivals). π in this table represents 180° or half period.

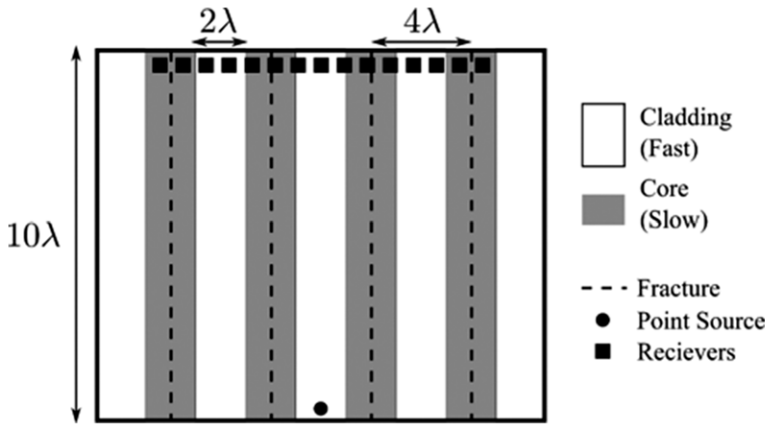

Fig. 19. Schematic of the computational set-up for sources and receivers. Sample geometries are given in Figures 20 and 21.

the two samples: more energy is contained in mode $m = 2$ for FV than in the direct wave and mode $m = 0$ wave than that observed for FH.

An unfractured TI medium with sub-wavelength layers does not support guided modes. As shown from the experiments and theory, the presence of parallel fractures in such a medium results in strong energy confinement between fractures, with the amount of confinement and arrival times of the guided modes dependent on fracture spacing, signal frequency, matrix properties and fracture specific stiffness.

In this section, as the layer thickness in the matrix is much smaller than a wavelength, the seismic response of the matrix can be simplified into a stiffness tensor by employing the effective medium approach. However, carbonate rocks with layer thicknesses larger than a wavelength are also encountered in a field. For that case, the layered matrix can no longer be treated as an effective medium. In the next section, we will examine P-wave guiding in an anisotropic medium with layer thicknesses of the order of 2λ and fracture spacing of the order of 4λ using computer simulations.

Fractured media with layer thicknesses greater than a wavelength

This section contrasts the analysis in the previous section (‘Fractured media with sub-wavelength layer thickness’) by assuming that the width of the layering in the bulk material is greater than a wavelength. In this limit, the bulk medium cannot be modelled as a homogeneous transversely isotropic material. Therefore, we computed the solutions with a computational domain that contains layers with different isotropic materials. It should be noted that for a given site, the bulk rock might display anisotropic behaviour for many reasons (e.g. layering, aligned microcracks, arrays of larger fractures and stylolites). However, for simplicity, the domains in this study only contain two types of layering that repeated periodically, with fracture dips parallel to the layering (Fig. 19). We used this configuration to prevent the obfuscation of wave solutions by multiple overlapping phenomena. To simulate a medium similar to Austin Chalk, a carbonate rock, the two different materials were chosen to match the wave speeds from laboratory measurements on Austin Chalk (Li 2011). The two materials will be referred to as the *cladding* and the *core* layers, and their properties are listed in Table 5. This nomenclature is based on the terminology used for light transmission along fibre optic cables. In a fibre optic cable, light is confined to the core by the contrast in index of refraction between the core and the material that surrounds and encases it (known as the cladding). For our study on compressional wave propagation in a layered medium, layers with slow wave speeds are refer to as core layers and the layers with fast wave speeds are referred to as the cladding layers.

In this section, the Discontinuous Galerkin (DG) method that was used to simulate isotropic

Table 5. *Material properties of the cladding (fast) and core (slow) media*

	Cladding medium	Core medium
P-wave velocity (m s^{-1})	3796	3464
S-wave velocity (m s^{-1})	2100	1900
Density (kg m^{-3})	2168	2038

elastic wave propagation is described. We use this approach to examine compressional-mode wave guiding in a layered medium both with and without fractures.

Numerical scheme: isotropic elastic wave equation

The DG method was used to compute numerically the propagation of isotropic elastic waves in the layered medium. The isotropic elastic wave equation is a linear hyperbolic equation, which is well suited for the DG method (Hesthaven & Warburton 2008). This method provides highly accurate solutions that enable waves to travel over multiple wavelengths with minimal dispersion (Dumbser & Käser 2006; Wilcox *et al.* 2010). We assume isotropic media and that each mesh element has constant material properties, such that the velocity-stress formulation can be written as:

$$\frac{\partial Q_{\mathrm{p}}}{\partial t} + A_{\mathrm{pq}}\frac{\partial Q_{\mathrm{q}}}{\partial x}, + B_{\mathrm{pq}}\frac{\partial Q_{\mathrm{q}}}{\partial y} = S_{\mathrm{p}}(t) \qquad (8)$$

where $Q_{\mathrm{p}} = (\sigma_{xx}, \sigma_{yy}, \sigma_{xy}, v_x, v_y)^{\mathrm{T}}$ is the solution vector (σ_{ij} is the (i, j) component of the stress tensor and v_i is the ith component of the particle velocity), $(A_{\mathrm{pq}}, B_{\mathrm{pq}})$ are the space-dependent Jacobian matrices, given by:

$$A_{\mathrm{pq}} = \begin{bmatrix} 0 & 0 & 0 & -(\lambda - 2\mu) & 0 \\ 0 & 0 & 0 & -\lambda & 0 \\ 0 & 0 & 0 & 0 & -\mu \\ -1/\rho & 0 & 0 & 0 & 0 \\ 0 & 0 & -1/\rho & 0 & 0 \end{bmatrix} \qquad (9)$$

$$B_{\mathrm{pq}} = \begin{bmatrix} 0 & 0 & 0 & 0 & -\lambda \\ 0 & 0 & 0 & 0 & -(\lambda - 2\mu) \\ 0 & 0 & 0 & -\mu & 0 \\ 0 & 0 & -1/\rho & 0 & 0 \\ 0 & -1/\rho & 0 & 0 & 0 \end{bmatrix} \qquad (10)$$

where λ and μ are the *Lamé constants*, and ρ is the mass density of the material. Note that Einstein summations are used in equation (8).

The DG construction used in this study will now be discussed; however, for an in-depth review see Dumbser & Käser (2006). The first step in deriving the DG method is to define the representation of the solution within each triangle. This is performed by expanding the approximated solution, Q_{h}, into a *trial* basis, Φ (Dumbser & Käser 2006):

$$(Q_{\mathrm{h}}^{(m)})_{\mathrm{p}}(\xi, \eta, t) = \hat{Q}_{\mathrm{h}}^{(m)}(t)\Phi(\xi, \eta) \qquad (11)$$

where (ξ, η) are the coordinates in a reference triangle, T_{R}. The reference triangle is defined by the coordinates: $((x_1, y_1) = (0, 0), (x_2, y_2) = (1, 0), (x_3, y_3) = (0, 1))$.

The Jacobi polynomials are a common choice of basis functions (Dumbser & Käser 2006). Next, the isotropic elastic wave equation is written in its weak form by first multiplying by a *test* function and then integrating over a single finite element, $T_{\mathrm{e}}^{(m)}$, of the domain. Since this is a Galerkin approximation, the *test* function is chosen from the basis functions that create the *trial* function space; that is, Φ in equation (11),

$$\int_{T_{\mathrm{e}}^{(m)}} \Phi_k \frac{\partial Q_{\mathrm{p}}}{\partial t}\,\mathrm{d}V + A_{\mathrm{pq}}\int_{T_{\mathrm{e}}^{(m)}} \Phi_k \frac{\partial Q_{\mathrm{p}}}{\partial x}\,\mathrm{d}V + B_{\mathrm{pq}}\int_{T_{\mathrm{e}}^{(m)}} \Phi_k \frac{\partial Q_{\mathrm{p}}}{\partial y}\mathrm{d}V = \int_{T_{\mathrm{e}}^{(m)}} \Phi_k S_{\mathrm{p}}(t)\,\mathrm{d}V. \qquad (12)$$

Then, the second and third terms are integrated by parts:

$$\int_{T_{\mathrm{e}}^{(m)}} \Phi_k \frac{\partial Q_{\mathrm{p}}}{\partial t}\,\mathrm{d}V + \int_{\partial T_{\mathrm{e}}^{(m)}} \Phi_k F_{\mathrm{p}}^h\,\mathrm{d}V - A_{\mathrm{pq}}\int_{T_{\mathrm{e}}^{(m)}} \frac{\partial \Phi_k}{\partial x} Q_{\mathrm{p}}\,\mathrm{d}V - B_{\mathrm{pq}}\int_{T_{\mathrm{e}}^{(m)}} \frac{\partial \Phi_k}{\partial y} Q_{\mathrm{p}}\,\mathrm{d}V = \int_{T_{\mathrm{e}}^{(m)}} \Phi_k S_{\mathrm{p}}(t)\,\mathrm{d}V. \qquad (13)$$

The second term in equation (13) introduces the numerical flux between elements that must be defined such that the system remains numerically stable and consistent. An upwinding numerical flux for a given triangle's edge was used (Dumbser & Käser 2006). It is written as:

$$F_{\mathrm{p}}^h = \frac{1}{2}T_{\mathrm{pq}}(A_{\mathrm{qr}}^{(m)} + |A_{\mathrm{qr}}^{(m)}|)T_{\mathrm{rs}}^{-1}\hat{Q}_{\mathrm{sl}}^{(m)}\Phi_{\mathrm{l}}^{(m)} + \frac{1}{2}T_{\mathrm{pq}}(A_{\mathrm{qr}}^{(m)} - |A_{\mathrm{qr}}^{(m)}|)T_{\mathrm{rs}}^{-1}\hat{Q}_{\mathrm{sl}}^{(m_j)}\Phi_{\mathrm{l}}^{(m_j)} \qquad (14)$$

where $\hat{Q}_{\mathrm{sl}}^{(m)}\Phi_{\mathrm{l}}^{(m)}$ and $\hat{Q}_{\mathrm{sl}}^{(m_j)}\Phi_{\mathrm{l}}^{(m_j)}$ are the boundary extrapolated values of the solution on element m and one of its three neighbours m_j $(j = 1, 2, 3)$, respectively. $A_{\mathrm{qr}}^{(m)}$ is the Jacobi matrix defined in equation (9) with the material properties of element m. $|A_{\mathrm{qr}}^{(m)}|$ is defined by deconstructing $A_{\mathrm{qr}}^{(m)}$ into its eigenvalues and vectors, then reconstructing it with the absolute values of the eigenvalues (Dumbser & Käser 2006). T_{pq} is a transformation matrix that rotates the system such that the

x-direction is aligned with the normal to an element's face:

$$T_{\mathrm{pq}} = \begin{bmatrix} n_x^2 & n_y^2 & -2n_x n_y & 0 & 0 \\ n_y^2 & n_x^2 & 2n_x n_y & 0 & 0 \\ n_x n_y & -n_x n_y & n_x^2 - n_y^2 & 0 & 0 \\ 0 & 0 & 0 & n_x & -n_y \\ 0 & 0 & 0 & n_y & n_x \end{bmatrix}. \quad (15)$$

Now that the spatial derivatives have been discretized, all that is left are the temporal derivatives. The computations for the temporal derivatives were accomplished with a Time Variation Diminishing (TVD) third-order Runge–Kutta method (Atkins & Shu 1998).

Simulation set-up

The computational domain is illustrated in Figure 19. Layers are aligned vertically and given a width of 7.24 mm (i.e. 2λ at 1 MHz). The domain was constructed by placing nine layers side-by-side, horizontally, such that each consecutive layer alternated from cladding to core and back to cladding (fast–slow–fast wave speeds). All of the embedded fractures were separated by the width of a layer, such that they were exclusively either in the cladding regions or in the core regions (Fig. 19). The material properties of the layers are given in Table 5. Unlike the work of De Basabe *et al.* (2011), linear-slip conditions are not implemented in the DG approach to simulate the reflection and transmission of waves across fractures. Instead, the fracture geometry is the source of the resulting seismic response from the fractures. The fractures were created by placing small diamond-shaped cracks equidistantly along the fracture plane. The cracks acted as if they were air filled by using free-surface boundary conditions. All of the cracks were 25 μm wide and 0.362 mm long (Fig. 20). By choosing the crack length to be much less than the wavelength, the fractures were in the displacement discontinuity limit (Kendall & Tabor 1971; Schoenberg 1980; Angel & Achenbach 1985). Five different stiffnesses were simulated by changing the contact area of the fracture. This was accomplished by adjusting the crack separation, d (Table 5). When the ratio of the wavelength to the crack separation increases (λ/d increases), the fracture specific stiffness also increases.

An explosive point source (represented by the excitation of the trace of the stress tensor) was placed within the central layer. A Ricker wavelet was used as an input to the point source, given as:

$$S(t) = A(0.5 + \pi f_c(t - t_o)^2)e^{-\pi f_c(t-t_o)^2} \quad (16)$$

where $A = 1$ is the amplitude, $t_o = 1$ μs is the source time delay and $f_c = 1$ MHz is the central frequency. This signal has a wavelength of 3.79 and 3.46 mm in the cladding and core layers, respectively. Note that the layer thickness is twice the average wavelength ($\lambda = c.$ 3.62 mm). A line of 300 equally spaced receivers were placed 10 wavelengths away from the source, at the top of the computational domain, to simulate the laboratory measurements such as those shown in Figure 1.

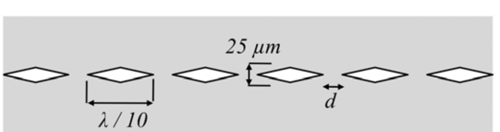

Fig. 20. Sketch of the equally spaced thin cracks used to model a fracture. The height (25 μm) and width ($\lambda/10 = c.$ 0.362 mm) of each crack remained constant for all simulations, and the crack separation, d, was varied (Table 5). Note that the height and width of the cracks are not drawn to scale.

Simulation results

Simulations were performed for an explosive source in an isotropic homogeneous domain (control case), in a homogeneous medium with fractures (control case), in a medium with alternating isotropic fast and slow velocity layers, and in a layered medium with fractures to determine the effect of fractures on wave guiding in a layered medium where the layer thickness and spacing are greater than a wavelength (Figs 21 & 22). The two control cases enabled the separation of the collected wave signals from the coupled systems. Figure 21 compares five different acoustic wavefronts when a source is located in the core layer (slow wave speed, see Table 6). In a homogenous isotropic medium (H-Co) with no layers or fractures, the wavefront spreads out uniformly in all directions (Fig. 21a) as expected. When fractures spaced 4λ apart are added to the

Table 6. *Simulation parameters*

Simulation name	No. of cracks	d	λ/d
Run 0 (control)	0	N/A	N/A
Run 2	17	1.8159 mm	1.945
Run 10	49	0.3801 mm	9.524
Run 25	71	0.1454 mm	24.896
Run 50	82	0.0772 mm	46.889
Run 100	90	0.0371 mm	97.536

Simulation names for different fracture specific stiffness generated by using a different number of cracks, crack separation, d, and the ratio of wavelength to crack separation, λ/d.

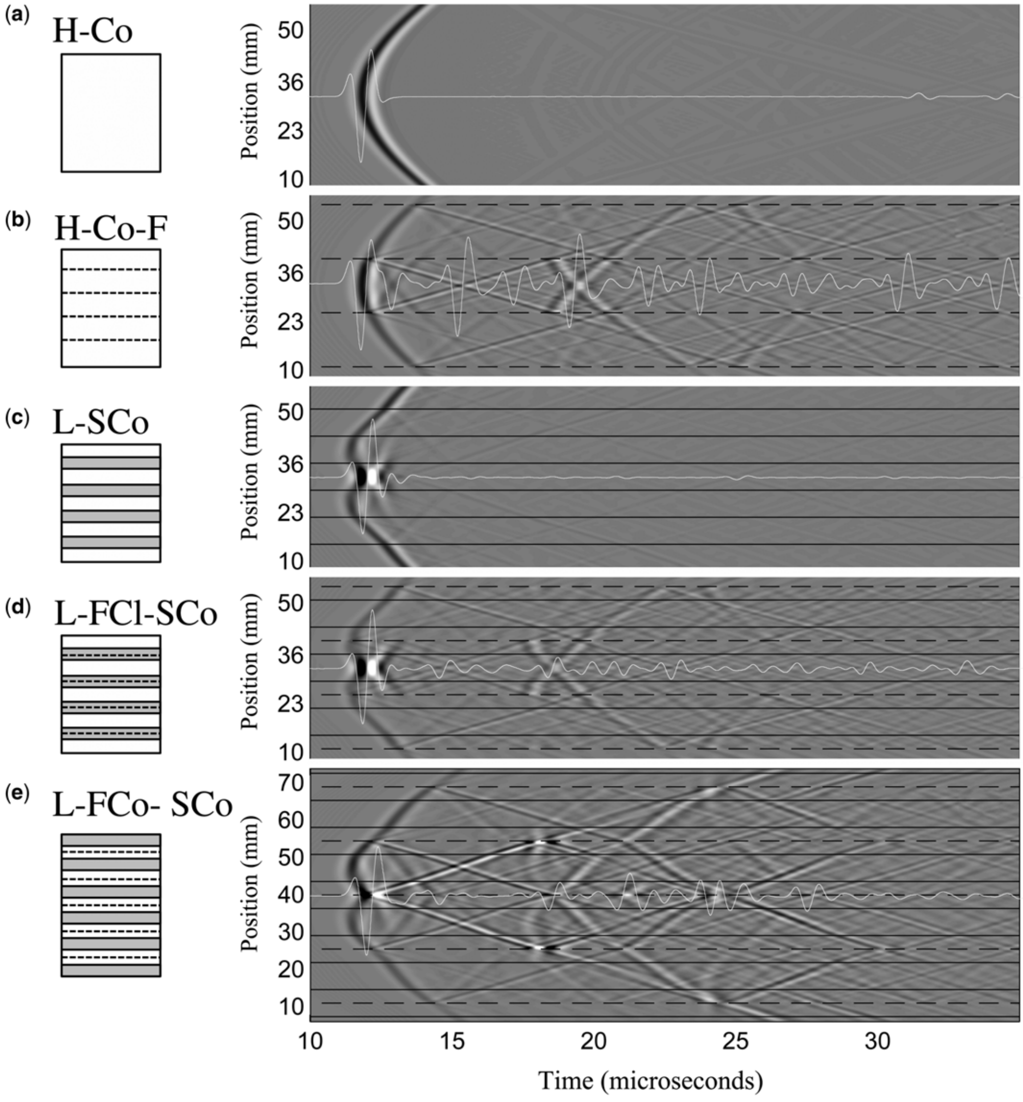

Fig. 21. Simulated wavefronts for compressional waves propagated in: (**a**) a slow homogeneous medium (H-Co); (**b**) the same as (a) but with fractures (H-Co-F); (**c**) a medium composed of alternating layers of isotropic cladding and core material (L-SCo); (**d**) same medium as (c) but with fractures (dashed line) located in the cladding layers (L-FCl-SCo); and (**e**) a medium composed of alternating layers of cladding and core material with fractures located in the core (L-FCo-SCp) layers. For these simulations, the source was located in a core layer (SCo). (See Table 6 for the P-wave speeds.) Fracture geometry is based on Run 2 for (b), (d) and (e).

homogeneous medium (H-Co-F in Fig. 21b), the wavefront is delayed when it crosses a fracture and reflected waves from the fracture are observed in the region between positions 25 and 40 mm, the location between the two central fractures. The first-arriving compressional wave is essentially the same for H-Co and H-Co-F. The signal from the H-Co-F only differs from the signal from H-Co around 12.5 μs when the first reflections from the fractures arrive (Fig. 21b). Strong energy confinement is not observed for H-Co-F.

Figure 21c–e compares and contrasts the wavefronts when layers are present (L-SCo), and two cases when both layers and fractures are present (L-FCl-SCo and L-FCo-SCo), to determine the effect of the location of the fractures on the wavefront and on the generation of guided modes. The acronym SCo stands for the source located in a

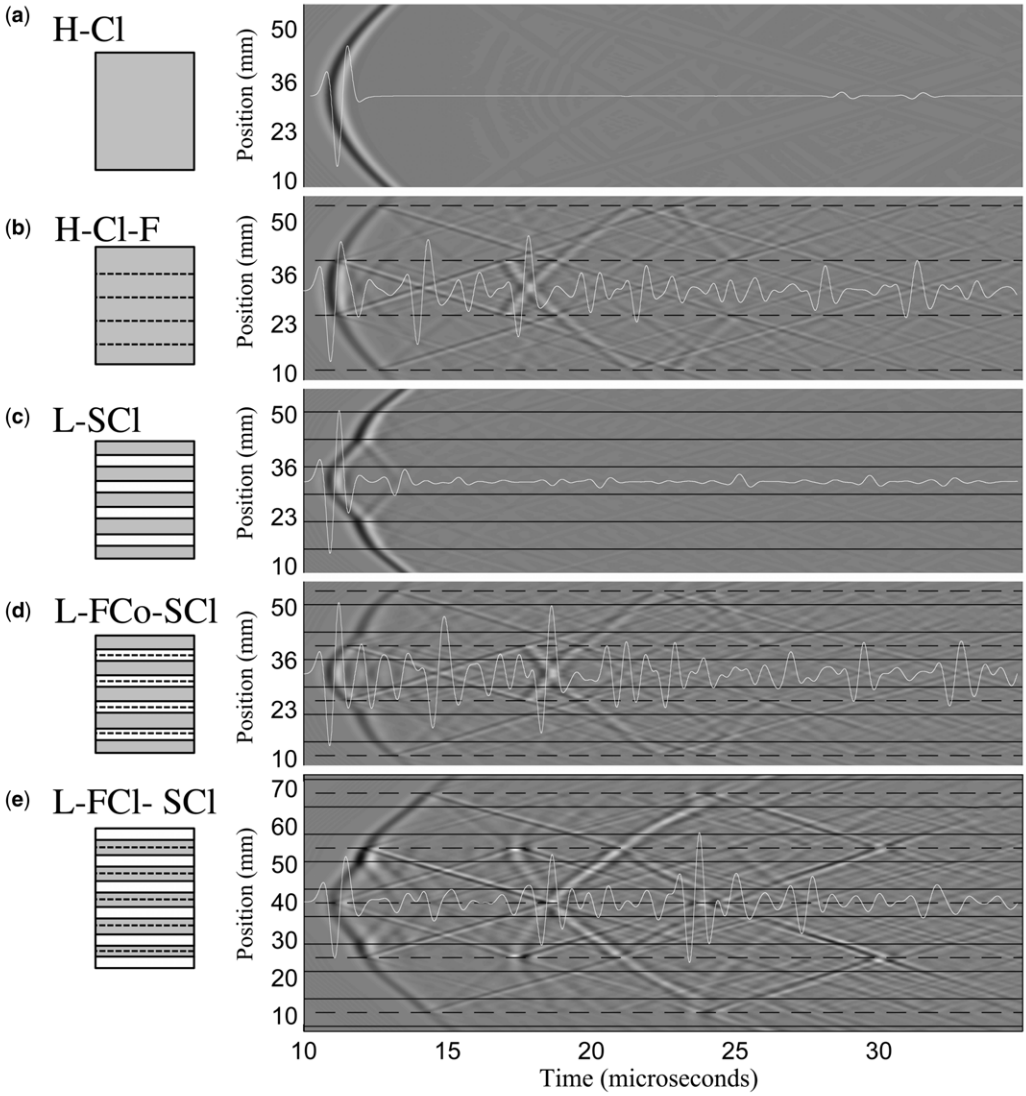

Fig. 22. Simulated wavefronts for compressional waves propagated in (**a**) a homogeneous cladding medium (H-Cl); (**b**) the same as (a) but with fractures (H-Cl-F); (**c**) a medium composed of alternating layers of isotropic cladding and core material (L-SCl); (**d**) same medium as (c) but with fractures (dashed line) located in the core (L-FCo-SCl) layers; and (**e**) a medium composed of alternating layers of cladding and core material with fractures located in the cladding (L-FCl-SCl) layers. For these simulations, the source was located in a cladding layer (SCl). (See Table 6 for P- and S-wave speeds.) Fracture geometry is based on Run 2 for (b), (d) and (e).

core layer (slow layer), FCl for when fractures are in the cladding layers and FCo for when fractures are in the core layers. For a layered medium without fractures (L-SCo in Fig. 21c), where the individual layers are isotropic but alternate between core and cladding media, the shape of the wavefront differs significantly from that in an isotropic medium (H-Co in Fig. 21a). The wave arrives earlier in the cladding medium than in the central core layer, resulting in a distorted wavefront. The alternating core–cladding layers cause energy confinement and results in compressional-mode wave guiding. The guided mode is confined by the velocity contrast (or impedance contrast – density × phase velocity) between the core and cladding layers. In Figure 23a, the peak-to-peak amplitude of L-SCo is 3 times larger than for the signals from H-Co and H-Co-F, which indicates wave-guiding

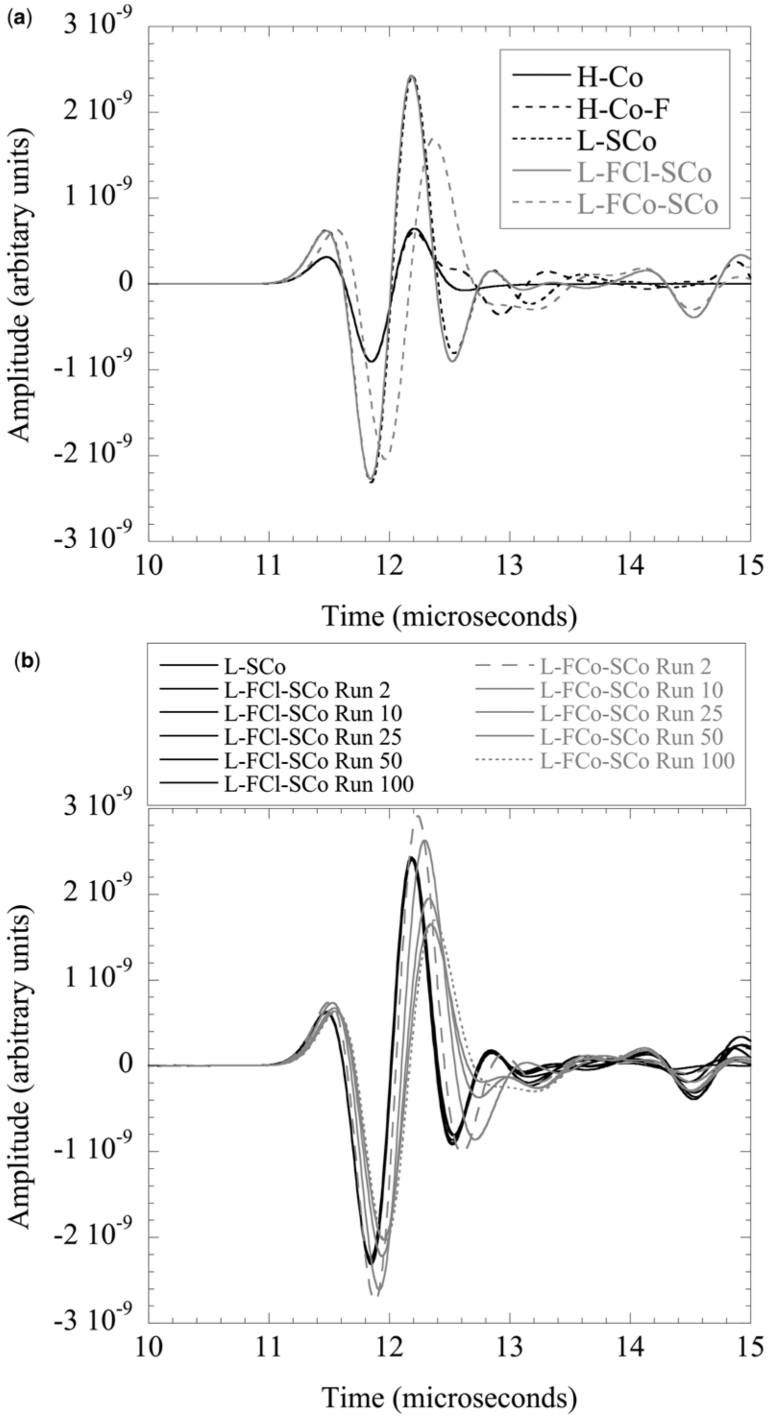

Fig. 23. (**a**) Signals showing first arrivals for signals taken from the centre of the wavefronts shown in Figure 21. (**b**) Signals from a layered medium with a source in the core (L-SCo), layered medium with fractures in cladding with a source in the core (L-FCl-SCo) and layered medium with fractures and source in the core (L-FCo-SCo) as fracture specific stiffness decreases (Run 2–Run 100).

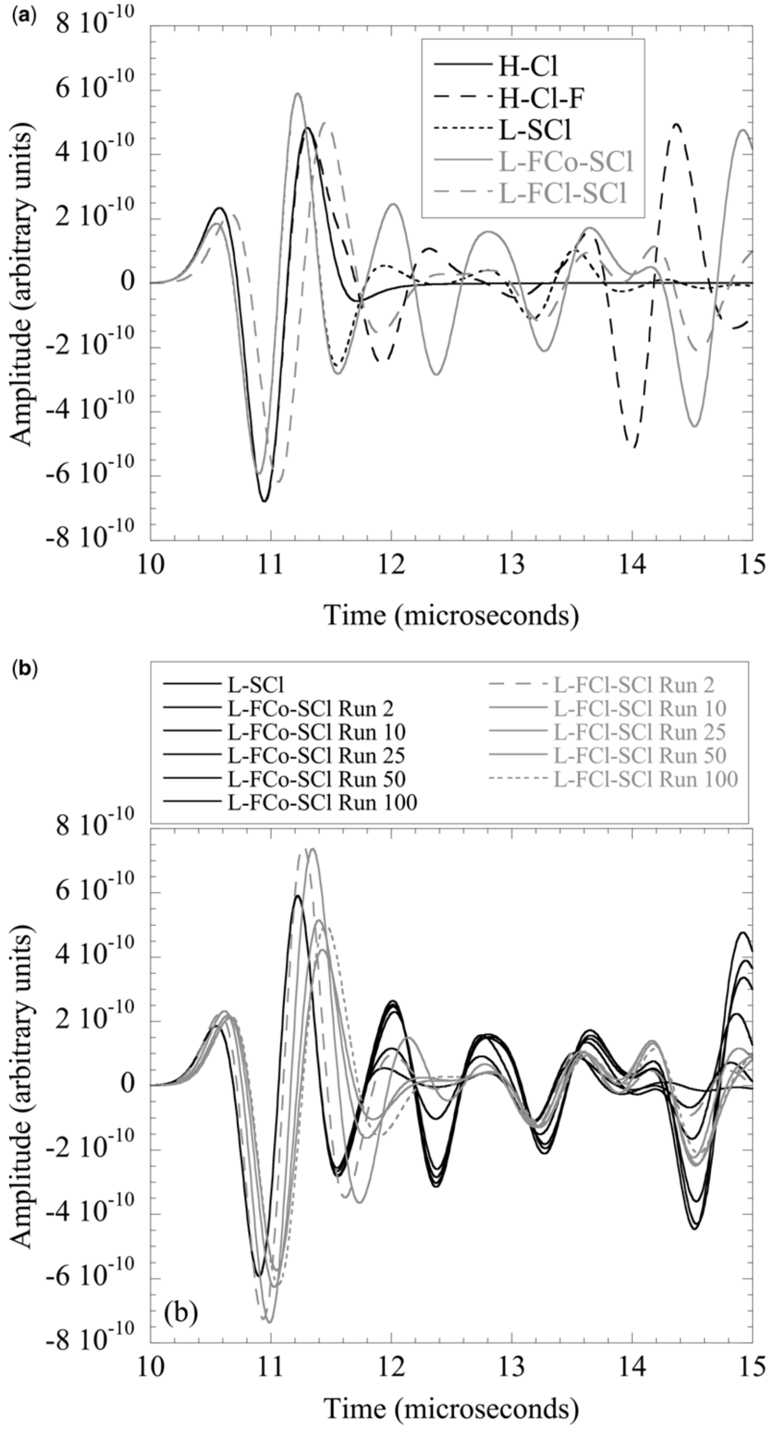

Fig. 24. (**a**) Signals showing first arrivals for signals taken from the centre of the wavefronts shown in Figure 22. (**b**) Signals from a layered medium with a source in the cladding (L-SCl), layered medium with fractures in the core with a source in the cladding (L-FCo-SCl) and layered medium with fractures and source in the cladding (L-FCl-SCl) as fracture specific stiffness decreases (Run 2–Run 100).

behaviour from constructive interference between the direct mode and the twice-reflected mode (see Fig. 2). When fractures are added to the cladding layers (L-FCl-SCo in Figs 21 & 23a), additional delays in the wavefront are observed as waves propagate across the fractures. But the first-arriving compressional mode is the same as that without fractures (Fig. 23a) and is insensitive to changes in fracture specific stiffness (Fig. 23b). The fractures are essentially invisible to the guided modes. However, when fractures are located within the core layers (L-FCo-SCo in Fig. 21e), the compressional-mode guided wave depends on fracture specific stiffness (Fig. 23b). The peak-to-peak amplitude of the guided mode in L-FCo-SCo is 2.4 times larger than that for H-Co and H-Co-F.

Whether the fractures enhance or suppress wave guiding relative to the layered case with no fractures depends on the stiffness of the fracture. For example, the guided mode for L-FCo-SCo Run 2 exhibits larger amplitudes than the layered unfractured case L-Sco, where the presence of the fractures increases the amount of energy in the guided mode. However, it is interesting to note that the amplitude of the guided mode decreases with decreasing fracture specific stiffness (decreases from Run 2 to Run 100 in Figs 23b & 24b) and wave guiding is suppressed relative to the layered case with no fractures. The decrease in amplitude (Fig. 25) arises from energy partitioning. Figure 25 shows an 8 μs window of the signal from the centre of the wavefront for simulation L-FCo-SCo. The arrival at 18 μs is the energy reflected from the fractures that are 4λ away from the centre of the wavefront. As the fracture stiffness decreases caused by a reduction in contact area (Kendall & Tabor 1971; Pyrak-Nolte & Cook 1987; Pyrak-Nolte & Morris 2000; Petrovitch *et al.* 2013), the reflected amplitude increases as expected for fractures (Pyrak-Nolte *et al.* 1990*a*). At 20.5 μs, a fracture interface wave is observed. Fracture interface waves are a form of a generalized Rayleigh wave that depends on the fracture specific stiffness and signal frequency (Murty 1975; Pyrak-Nolte & Cook 1987; Pyrak-Nolte *et al.* 1992*a*, *b*, 1996; Gu 1994; Gu *et al.* 1996; Nihei *et al.* 1997; Shao & Pyrak-Nolte 2013). The velocity of fracture interface waves ranges between the Rayleigh velocity at low fracture specific stiffness (when a fracture behaves as a free surface) and the bulk shear wave velocity (when a fracture behaves as a welded contact). For simulation L-FCo-SCo, the amplitude of the observed fracture interface wave increases with decreasing fracture stiffness. The decrease in amplitude of the guided compressional mode with decreasing stiffness results from energy partitioning into this fracture interface wave. Thus, while one would expect increased energy confinement of

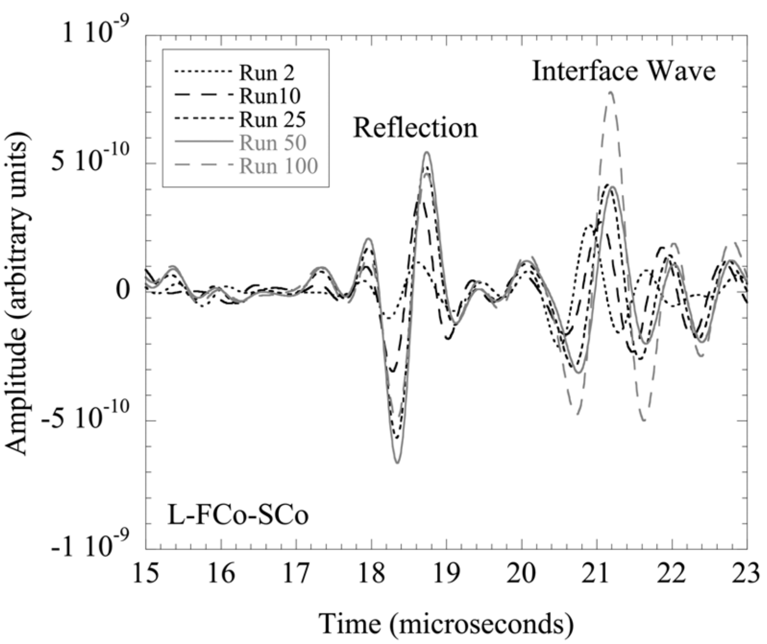

Fig. 25. Signals from a simulation of a layered medium with fractures and source in the core (L-FCo-SCo) as fracture specific stiffness decreases (Run 2 – Run 100) showing the arrival of a mode reflection from fractures located at positions 35 mm and 55 mm, and an interface wave guided by the fracture in the source core layer.

compressional guided mode to increase as the fracture specific stiffness decreases, the partitioning of energy into a fracture interface wave mode results in the opposite behaviour.

Figure 22 compares the wavefront for five cases when the source is in a cladding (fast) layer (SCl). As for H-Co, the wavefront from H-Cl spreads out uniformly in the isotropic medium (Fig. 22a). When fractures are present, the wavefront is only delayed when it crosses a fracture (Fig. 22b) and numerous reverberations are observed from the fractures. When a source is located in the cladding for layered medium L-SCl (Fig. 22c), energy confinement in the cladding layer is not significant as expected for a high-velocity layer surrounded by low-velocity layers. When sources are located in the cladding for the fractured media L-FCo-SCl and L-FCL-SCl (Fig. 22d, e), energy confinement in the cladding layer is also not significant. A comparison of the signals (Fig. 24a) from the centre wavefronts for these samples shows that the peak-to-peak amplitudes are within $\pm 3\%$ of the homogenous case (H-Cl). Launching a wave in the cladding for either case L-FCo-SCl or L-FCL-SC leads to suppression of wave guiding. Only the first arrival for L-FCL-SCl exhibits sensitivity to changes in fracture specific stiffness.

Conclusion

Reservoir management relies on geological modelling and flow simulations that require information on the matrix properties of the rock formations, and the identification of fractures or fracture networks. Matrix properties can be obtained from borehole and core analyses but the identification and characterization of fractures is often more difficult. Fractures in carbonate rock are known to vary in size, number, orientation, spacing and connectivity because of depositional and diagenetic processes, as well as from tectonic processes during and after formation. Typically, seismic reservoir characterization techniques or cross-well studies use body wave methods such as shear-wave splitting and azimuthal compressional-wave attributes for fracture location and orientation. These methods lead to interpretation of directionally dependent properties but cannot easily separate out the contribution to the anisotropy from the rock matrix (from texture porosity, mineralogy, cement and microcracks) and that from the fractures. This information is important when trying to determine whether a reservoir system is dominated by either fluid flow in fractures or fluid flow through the matrix or a combination of the matrix–fracture interaction.

Based on the results of this research, the measurement and interpretation of guided modes has the potential to identify both the matrix and fracture-induced anisotropy. Compressional waves guided by impedance contrasts have been used in cross-well studies in oil-bearing sand–shale reservoirs (Leary *et al.* 2005), coal seams (Buchanan *et al.* 1983) and sandstone–shale formations (Parra *et al.* 2002) for distances greater than 600 m for a frequency range of 50–350 Hz. To apply these techniques to fractured carbonate reservoir characterization requires an understanding that fractures can produce wave guiding, and the behaviour of the guided modes depends on contributions from the mechanical properties of both the fracture and the matrix.

In this paper, we examined the behaviour of compressional wave guided modes to obtain information on the properties of fractures in layered media. For a transversely isotropic medium with sub-wavelength layers, we demonstrated theoretically and experimentally that guided modes can be used to determine the orientation of a fracture set relative to the layering in the matrix from interpretation of time delays of later arriving modes. Fractures support guided modes that are guided by the fracture orientation, depend on fracture spacing and the properties of the fractures (e.g. fracture specific stiffness) and on the frequency of the signal. In addition, we showed that the arrival times of these guided modes are also affected by the anisotropy of the matrix through the directional dependence of the compressional and shear wave velocities. In our study, guided modes in fractured anisotropic media existed with significant energy over distances comparable to 25 wavelengths for frequencies between 0.5 and 1 MHz. For the frequencies mentioned above for the cross-well studies and typical compressional wave speeds in carbonate rock (4000–6000 m s^{-1}), guided modes with significant energy should be observable at distances of 300–3000 m depending on the fracture specific stiffness (of the order of 10^6–10^{10} Pa m^{-1}).

Interpretation of fracture properties from guided modes in fracture anisotropic rock is aided by the seismic response of fractures. Whether in the field or the laboratory, the best methods for detecting and characterizing fractures requires a ‘trajectory’ along a variable that is affected by the condition of the fractures. For example, in the laboratory, a stress trajectory or loading path is often used to open and close a fracture; that is, to decrease or increase the fracture specific stiffness. This, in turn, affects reflection and transmission coefficients and group time delays, as well as the spectral content of the signal. Conversely, a broadband source–receiver set-up can be used for a fracture sample under a constant static load. Spectral analysis shows that for the same fracture specific stiffness, high-frequency components of the signal will be more strongly attenuated and exhibit smaller time delays than low-frequency components (i.e. dispersion). For the guided modes studied in this paper, identification of the fracture orientation relative to the matrix and characterization of the fracture properties at cross-hole or field frequencies would require broad-band sources and receivers, and spectral analysis of the data. Spectral analysis would provide the time dispersion that aids in the identification of guided modes and is also a link to the stiffness of the fractures and to the fracture spacing. Future controlled field studies are needed to achieve the full potential of guided modes for interpreting fracture and matrix properties in carbonate rock.

This work is supported by the Geosciences Research Program, Office of Basic Energy Sciences, US Department of Energy (DE-FG02-09ER16022), by the Geo-Mathematical Imaging Group at Purdue University, the Purdue Research Foundation and the Computer Research Institute at Purdue University. The authors also thank Dr J. Neilson for her generous help on carbonate geology.

References

Aki, K. & Richards, P. G. 2005. *Quantitative Seismology*, 2nd edn. University Science Books, Sausalito, CA.

Angel, Y. & Achenbach, J. 1985. Reflection and transmission of elastic waves by a periodic array of cracks. *Journal of Applied Mechanics*, **52**, 33–41.

Atkins, H. L. & Shu, C. W. 1998. Quadrature-free implementation of discontinuous Galerkin method for hyperbolic equations. *AIAA Journal*, **36**, 775–782.

Backus, G. E. 1962. Long-wave elastic anisotropy produced by horizontal layering. *Journal of Geophysical Research*, **67**, 4427–4440.

Barton, N. R., Bandis, S. & Bakhtar, K. 1985. Strength, deformation and conductivity coupling of rock joints. *International Journal of Rock Mechanics and Mining Sciences*, **22**, 121–140.

Boggs, S. 2006. *Principles of Sedimentology and Stratigraphy*, 4th edn. Prentice Hall, Englewood Cliffs, NJ.

Brown, S. R. & Scholz, C. H. 1985. Closure of random elastic surfaces in contact. *Journal of Geophysical Research*, **90**, 5531–5545.

Brown, S. R., Kranz, R. L. & Bpnner, B. P. 1986. Correlation between surfaces of natural rock joints. *Geophysical Research Letters*, **13**, 1430–1434.

Buchanan, D. J., Jackson, P. J. & Davis, R. 1983. Attenuation and anisotropy of channel waves in coal seam. *Geophysics*, **163**, 133–147.

Carcione, J. M. & Picotti, S. 2012. Reflection and transmission coefficients of a fracture in transversely isotropic media. *Studia Geophysica et Geodaetica*, **56**, 307–322.

De Basabe, J. D., Sen, M. K. & Wheeler, M. F. 2011. Seismic wave propagation in fractured media: a discontinuous Galerkin approach. In: *Society of Exploration Geophysicists Annual Meeting, San Antonio, Texas, 18–23 September*. Society of Exploration Geophysicists, Tulsa, OK, 2921–2924.

Dumbser, M. & Käser, M. 2006. An arbitrary high-order Discontinuous Galerkin method for elastic waves on unstructured meshes – II. The three-dimensional isotropic case. *Geophysical Journal International*, **167**, 319–336.

Fatemi, S. M. & Kharrat, R. 2012. The effect of fractures' geometrical properties on the recovery mechanisms of the top-down in situ combustion process. *Petroleum Science and Technology*, **30**, 147–158.

Gu, B. L. 1994. *Interface waves on a fracture in rock*. PhD thesis, University of California, Berkeley, CA.

Gu, B. L., Nihei, K. T., Myer, L. R. & Pyrak-Nolte, L. J. 1996. Fracture interface waves. *Journal of Geophysical Research: Solid Earth*, **101**, 827–835.

Hesthaven, J. S. & Warburton, T. 2008. *Nodal Discontinuous Galerkin Methods*. Springer, New York.

Hopkins, D. L. 1990. *The effect of surface roughness on joint stiffness, aperture and acoustic wave propagation*. PhD thesis, University of California, Berkeley, CA.

Hopkins, D. L., Cook, N. G. W. & Myer, L. R. 1987. Fracture stiffness and aperture as a function of applied stress and contact geometry. *In*: *Proceedings of the 28th US Symposium on Rock Mechanics, University of Arizona, Tucson, Arizona*. A.A. Balkema, Rotterdam.

Hopkins, D. L., Cook, N. G. W. & Myer, L. R. 1990. Normal joint stiffness as a function of spatial geometry and surface roughness. *In*: Barton, W. & Stephansson, E. (eds) *International Symposium on Rock Joints, Loen, Norway*. A.A. Balkema, Rotterdam, 203–210.

Kendall, K. & Tabor, D. 1971. An ultrasonic study of Area of Contact between Stationary and Sliding Surfaces. *Proceedings of the Royal Society of London Series A – Mathematical and Physical Sciences*, **323**, 321–340.

Kitsunezaki, C. 1983. Behaviour of plane waves across a plane crack. *Journal of the Mining College, Akita University Series A*, **3**, 173–187.

Leary, P. C., Ayres, W., Yang, W. J. & Chang, X. F. 2005. Crosswell seismic waveguide phenomenology of reservoir sands and shales at offsets >600 m, Liaohe Oil Field, NE China. *Geophysical Journal International*, **163**, 285–307.

Li, W. 2011. *Seismic wave propagation in fractured Anisotropic Carbonate Rock: Experiments and Theory*. PhD thesis, Purdue University, West Lafayette, IN.

Li, W., Petrovitch, C. & Pyrak-Nolte, L. J. 2009. The effect of fabric-controlled layering on compressional and shear wave propagation in carbonate rock. *International Journal of the Japanese Committee for Rock Mechanics*, **4**, 79–85.

Lubbe, R., Sothcott, J., Worthington, M. H. & McCann, C. 2008. Laboratory estimates of normal and shear fracture compliance. *Geophysical Prospecting*, **56**, 239–247.

Murty, G. S. 1975. A theoretical model for the attenuation and dispersion of Stoneley waves at the loosely bonded interface of elastic half-spaces. *Physics of the Earth and Planetary Interiors*, **11**, 65–79.

Nihei, K. T., Gu, B. L., Myer, L. R., Pyrak-Nolte, L. J. & Cook, N. G. W. 1997. Elastic interface wave propagation along a fracture. *In*: *Proceedings of the Eighth ISRM Congress on Rock Mechanics, Tokyo, Japan, 25–29 September, Volume 3*. A.A. Balkema, Rotterdam, 1151–1157.

Nihei, K. T., Yi, W., Myer, L. R. & Cook, N. G. W. 1999. Fracture channel waves. *Journal of Geophysical Research: Solid Earth*, **10**, 4749–4781.

Oliger, A., Nolte, D. D. & Pyrak-Nolte, L. J. 2003. Seismic focusing by a single planar fracture. *Geophysical Research Letters*, **30**, 71–74.

Parra, J. O., Hackert, C. L., Gorody, A. W. & Korneev, V. 2002. Detection of guided waves between gas wells for reservoir characterization. *Geophysics*, **67**, 38–49.

Petrovitch, C. L., Nolte, D. D. & Pyrak-Nolte, L. J. 2013. Scaling of Fluid Flow versus Fracture Stiffness. *Geophysical Research Letters*, **40**, 2076–2080.

Pyrak-Nolte, L. J. & Cook, N. G. W. 1987. Elastic interface waves along a fracture. *Geophysical Research Letters*, **14**, 1107–1110.

Pyrak-Nolte, L. J. & Morris, J. P. 2000. Single fractures under normal stress: The relation between fracture stiffness and fluid flow. *International Journal of Rock Mechanics and Mining Sciences*, **37**, 245–262.

Pyrak-Nolte, L. J., Myer, L. R. & Cook, N. G. W. 1990*a*. Transmission of Seismic-Waves across Single Natural Fractures. *Journal of Geophysical Research: Solid Earth and Planets*, **95**, 8617–8638.

Pyrak-Nolte, L. J., Myer, L. R. & Cook, N. G. W. 1990*b*. Anisotropy in seismic velocities and amplitudes from multiple parallel fractures. *Journal of Geophysical Research: Solid Earth and Planets*, **95**, 11,345–11,358.

Pyrak-Nolte, L. J., Xu, J. P. & Haley, G. M. 1992*a*. Elastic interface waves along a fracture – theory and experiment. *In*: Tillerson, J. R. & Wawersik, W. R. (eds) *Rock Mechanics: Proceedings of the 33rd US Symposium, Sante Fe, New Mexico, 3–5 June 1992*. A.A. Balkema, Rotterdam, 999–1007.

Pyrak-Nolte, L. J., Xu, J. P. & Haley, G. M. 1992*b*. Elastic interface waves propagating in a fracture. *Physical Review Letters*, **68**, 3650–3653.

Pyrak-Nolte, L. J., Roy, S. & Neumann, C. 1996. Incipient interface waves used to monitor rock failure. *In*: Aubertin, M., Hassani, F. & Mitri, H. (eds) *Rock Mechanics: Tools and Techniques: Proceedings of the 2nd North American Rock Mechanics Symposium, NARMS'96, Montreal, Quebec, 19-21 June 1996, Volumes 1 and 2*. Balkema, Rotterdam, 1169–1175.

Roy, S. & Pyrak-Nolte, L. J. 1995. Interface waves propagating along tensile fractures in dolomite. *Geophysical Research Letters*, **22**, 2773–2776.

Saleh, B. E. & Teich, M. C. 1991. *Fundamentals of Photonics*. Wiley, New York.

Schoenberg, M. 1980. Elastic wave behaviour across linear slip interfaces. *Journal of the Acoustical Society of America*, **5**, 1516–1521.

Sheriff, R. E. & Geldart, L. P. 1995. *Exploration Seismology*, 2nd edn. Cambridge University Press, Cambridge.

Shao, S. & Pyrak-Nolte, L. J. 2013. Interface waves along fractures in anisotropic media. *Geophysics*, **78**, 99–112.

Thomsen, L. 1986. Weak elastic anisotropy. *Geophysics*, **51**, 1954–1966.

Wilcox, L. C., Stadler, G., Burstedde, C. & Ghattas, O. 2010. A high-order discontinuous Galerkin method for wave propagation through coupled elastic-acoustic media. *Journal of Computational Physics*, **229**, 9373–9396.

Wolfe, J. P. 1995. Acoustic wavefronts in crystalline solids. *Physics Today*, **48**, 34–40.

Xian, C. 2001. *Wavefront imaging of energy confinement by multiple parallel fractures*. Master thesis, Purdue University, West Lafayette, IN.

Xian, C. J., Nolte, D. D. & Pyrak-Nolte, L. J. 2001. Compressional waves guided between parallel fractures. *International Journal of Rock Mechanics and Mining Sciences*, **38**, 765–776.